Validation of New Operational Package for the Lagrangian Diagnosis of Stratosphere-Troposphere Exchange

by

AYAKO YAMAMOTO

Department of Atmospheric and Oceanic Sciences

McGill University
Montreal, Canada
September 2011

A thesis submitted to the Faculty of Graduate Studies and Research in partial fulfillment of the requirements for the degree of Master of Science

Acknowledgement

First and foremost, this thesis would not have been possible without my supervisors, Prof. Michel Bourqui and Prof. Seok-Woo Son, whose encouragement, guidance and support throughout this project enabled me to develop an understanding of the subject. Having been able to work under their supervision was such an exciting, inspiring and great experience in many, many ways. I would also like to thank David Tarasick for giving me the opportunity to take part in an ozonesonde campaign, which was truly a dream-come-true experience for me. Thank you also to everyone who took part in the campaign, with special thanks to Louis, Ron, Jonathan and Ildiko for their positivity which made the campaign exciting and successful. I am also grateful to the members of stratospheric dynamics and chemistry group and of climate dynamics group for their insightful inputs and to the administrative staffs of the department for their friendly assistance. My special appreciation goes to my parents, who always have a faith in me and let me take my own path. I can keep going as you always remind me that I have a home I can always return to. Last but not least, I owe my heartiful gratitude to Patrick, my boyfriend as well as my teacher of matlab, Latex and French, for providing me ongoing support and love, and comfort with beavertails from time to time.

Abstract

A new tool for the Lagrangian diagnosis of stratosphere-troposphere exchange (STE) was developed for Environment Canada and became operational in July 2010, providing unique, high-resolution daily forecasts of STE over the globe. This thesis offers a comprehensive validation of these STE forecasts in the context of an ozonesonde balloon campaign conducted at three locations in Eastern Canada from 12 July to 4 August 2010. The STE forecasts are calculated using a Lagrangian kinematic trajectory methodology based on the high-resolution global GEM model forecasts at Environment Canada. Both observations and the STE forecasts during this period showed much larger frequency of stratospheric air intrusions deep into the troposphere at all locations compared to past studies. The STE dataset compares reasonably well with the observations above 500 hPa, yet is found to underestimate the frequency of events reaching below 700 hPa level. Sources of error can possibly be introduced by (1) errors in the 6-day global GEM forecasts, (2) errors in the identification of air with stratospheric origin in observations, and/or (3) the lack of convective and turbulent mixing representation in the trajectory model. Despite these large sources of errors, the STE forecasts turn out to be one of the best datasets available for the STE studies, being useful to estimate

the currently controversial STE contribution to the tropospheric ozone budget in the free troposphere as well as in the boundary layer.

Résumé

Un nouvel outil de diagnostic d'échange stratosphère-troposphère (STE) a été développé pour Environment Canada et est devenu opérationnel en Juillet 2010, fournissant des prévisions quotidiennes de haute résolution à l'échelle globale. Cette thèse offre une validation complète des prévisions STE dans le contexte d'une campagne de ballons-sondes mesurant l'ozone, conduite à trois localisations dans l'Est du Canada du 12 Juillet au 4 Août 2010. Les prévisions STE sont calculées avec une méthode cinématique de trajectoires Lagrangiennes basée sur la sortie du modèle global à haute résolution GEM d'Environment Canada. Les observations et résultats du modèle montrent une fréquence d'intrusions profondes d'air stratosphérique bien plus grande que dans les études précédentes. Les données STE correspondent relativement bien aux observations au dessus de 500 hPa, mais elles sous-estiment la fréquence des évènements attaignant 700 hPa. Les sources d'erreurs sont possiblement: (1) des erreurs dans la prévision de GEM, (2) des erreurs dans l'identification de parcelle d'air d'origine stratosphérique et/ou (3) le manque de convection et de turbulence dans le modèle de trajectoire. Malgré ces sources d'erreurs, les données d'intrusions s'avèrent être une des meilleures sources disponible pour, entre autres, estimer la présente et controversée contribution stratosphérique

au budget total d'ozone de la troposphère.

Contents

List of Figures

List of Tables

Chapter 1

Introduction

1.1 Structure and composition of the atmosphere

The Earth's atmosphere can be divided into different layers that differ in their chemical, physical, and dynamical properties. For instance, according to the thermal structure, the atmosphere can be decomposed into *troposphere*, *stratosphere*, *mesosphere*, and *thermosphere* from the surface upwards.

In the *troposphere*, the lowest of all, the temperature generally decreases with height until it reaches the tropopause, reflecting a low static stability and the presence of convection. On average it contains 99 % of the moisture content as well as 80 % of the whole Earth's atmospheric mass. Consequently, as the name troposphere suggests, this region is signified with *turning* (or vertical mixing) and allows virtually all weather phenomena we experience everyday. Thus the chemical species tend to be vertically homogeneous in the troposphere. The planetary boundary layer (PBL), located in the lowest part of the troposphere, is a layer of enhanced turbulence due to its proximity to the surface. Its depth is variable but to a rough approximation corresponds to the lowest 1 - 2 km of the troposphere and this is where almost all anthropogenic chemical species are produced. At the top of PBL, there frequently occur temperature inversions which can trap anthropogenic species close to the surface.

Above the troposphere lies a statically stable and dry layer called the *stratosphere*. In this region of the atmosphere the temperature increases with height due to the presence of ozone. Ozone is mainly produced in the tropical stratosphere as a result of photo-dissociation of oxygen molecules (O_2) by insolation into highly reactive atomic oxygen (O), which quickly reacts with oxygen molecules (O_2) to form ozone (O_3). Then by the stratospheric mean meridional circulation known as Brewer-Dobson circulation (Brewer 1949; Dobson 1956), it is transported from the tropics to the middle and high latitudes and downward into the lower stratosphere. Ozone has longer lifetime in the higher latitudes due to lower ultraviolet radiation, which is essential to drive catalytic reactions to destroy ozone molecules. As a consequence of both transport and photochemistry, the largest concentrations of ozone are found in the high latitude lower stratosphere. In this so-called ozone layer, ozone molecules absorb ultraviolet solar radiation and convert it into molecular kinetic energy, which represents the main heat source for the stratosphere.

Therefore, in contrast to the troposphere, where the moisture is abundant and ozone is more scarce, the stratosphere is very dry yet very rich in ozone. Also due to its large positive static stability, time scales of the vertical transport of mass and chemical constituents are much longer in the stratosphere. Indeed, it takes years to cross the stratosphere via the residual circulation, in contrast to the troposphere where the time scales are as short as hours via moist convection or days via baroclinic eddy motions (Holton et al. 1995).

1.2 Tropopause definitions and STE

The tropopause separates these two lowest atmospheric layers with very different chemical and dynamical properties. It is not a fixed boundary but rather highly variable in time and space, and there exist a few different definitions: Namely, *thermal*, *dynamical*, and *ozone tropopause*.

The *thermal tropopause* is defined by World Meteorological Organization (WMO 1986) as "the lowest level at which the temperature lapse rate decreases to 2 Kkm^{-1} or less and the average lapse rate between this level and any other levels within 2 km does not exceed 2 Kkm^{-1}". This can be inferred from a single temperature profile. The tropopause thus defined, however, breaks down around the jet stream region.

The *dynamical tropopause* is typically defined using potential vorticity (PV), which is given by

$$PV = \frac{1}{\rho}\zeta_a \cdot \nabla\theta, \tag{1.1}$$

where ρ is the air density, θ is the potential temperature, and $\zeta_a = f\mathbf{k} + \nabla \times \mathbf{v}$ is the absolute vorticity with Coriolis parameter f, the unit vector in the vertical direction $\mathbf{k}$ as well as the horizontal wind $\mathbf{v}$ (Hoskins et al. 1985). Owing to the high static stability in the stratosphere, the PV field there takes larger values than in the troposphere. As a result the tropopause makes the transition with particularly large PV gradients.

The above two definitions are however not separate. In fact, the thermal tropopause in extratropics is known to coincide with constant PV surfaces (Hoskins et al. 1985), with the value of 2 PVU being commonly used (where $1PVU = 10^{-6} Km^2 kg^{-1} s^{-1}$), albeit various choices of PV values are used in the literature ranging from 1.6 PVU to 3.5 PVU (Stohl et al. 2003). Despite this arbitrariness of the choice of PV surface and the small-scale systematic biases observed compared to the thermal tropopause (Wirth 2000), the dynamical tropopause definition is often preferred over the thermal counterpart in the extratropics, mainly because of its quasi-materialistic nature under adiabatic, frictionless conditions (Hoskins et al. 1985). In the tropics, where PV surfaces may extend to infinite height, the thermal tropopause corresponds well with the 380-K potential temperature surface (Holton et al. 1995).

Another emerging definition is with use of ozone, which displays a strong transition of the ozone concentrations due to the observed low value in the troposphere in contrast to the high value in the stratosphere. Bethan et al. (1996) found from their analysis with over six hundred profiles that the ozone tropopause tends to almost always lie lower than thermal counterpart on average by about 800 m.

Regardless of the definitions applied, however, the tropopause is not an absolute lid that completely separates the troposphere and the stratosphere, but there occur exchanges between the two regions of the atmosphere known as *stratosphere – troposphere exchange* (*STE*) *events*. Due to the extremely different natures of those two layers, STE can cause significant impacts on both regions, by perturbing their chemical compositions and in turn their radiative and chemical balances. Transport of anthropogenic species from the troposphere into the stratosphere is known to affect stratospheric chemistry, with ozone depletion being its most striking illustration. On the other hand, transport of stratospheric air into the troposphere injects ozone, which is harmful for human's health and also largely contributes to the tropospheric cleansing mechanism, oxidizing and neutralizing toxic pollutants emitted at the surface of the Earth.

There have been numerous studies focusing on STE, with one of its first observations being done by Danielsen (1968). They conducted analysis by measuring radioactive fallout debris of the nuclear bomb test, along with water vapour and ozone, and confirmed the studies by Reed (1955) and Reed and Danielsen (1959) who identified stratospheric air both in the middle and upper troposphere, using potential vorticity as a quasi-conservative tracer.

1.3 STE in the context of large-scale circulation

There are mainly two views to look at the STE: On the one hand as a part of the global-circulation picture, and on the other hand through the smaller-scale processes driving the transport across dynamical tropopause. For the sake of convenience, hereafter the notion of STT is used for the downward stratosphere-to-troposphere transport, and TST for the reverse transport, following Stohl et al. (2003).

In the former, the large-scale circulation is driven nonlocally by Rossby and gravity waves breaking in the extratropical middle stratosphere (Holton et al. 1995). In the tropics the air is brought upward and then poleward and downward in the extratropics. Hoskins (1991) proposed to view STE in this framework and separate the lower stratosphere and the upper troposphere into three different layers: *overworld*, *middleworld* and *underworld*. Figure 1-1, excerpted from Holton et al. (1995), gives the overview of the picture. The overworld is defined as the region above the 380 K isentropic surface and lies fully in the stratosphere. The transport from this region to the troposphere is restricted to be only by diabatic cooling, as the isentropes are not crossing the tropopause. The middleworld is where isentropes cross the tropopause, and is located in the troposphere near the tropics and in the stratosphere closer to the pole. This is where the most efficient exchanges can occur by quasi-adiabatic processes along isentropic surfaces in both direction (Chen 1995), but dominantly STT. The underworld is the lowermost region where the entire isentropic surfaces lie in the troposphere. Diabatic heating is the only process which can bring the air from this region into the stratosphere (Stohl et al. 2003). Thus Holton et al. (1995) concluded that it is sufficient to look at the transport across the 380 K isentropic surface to evaluate the net global STE rather than across the tropopause. Indeed this picture clarifies the different processes (diabatic vs. adiabatic processes) related to different region of the lower stratosphere as described above; however, as Stohl et al. (2003) argued, there are three limitations to these global estimates:

1. They are spatially averaged, normally over the hemisphere,

2. they are temporally averaged, normally over a month, and

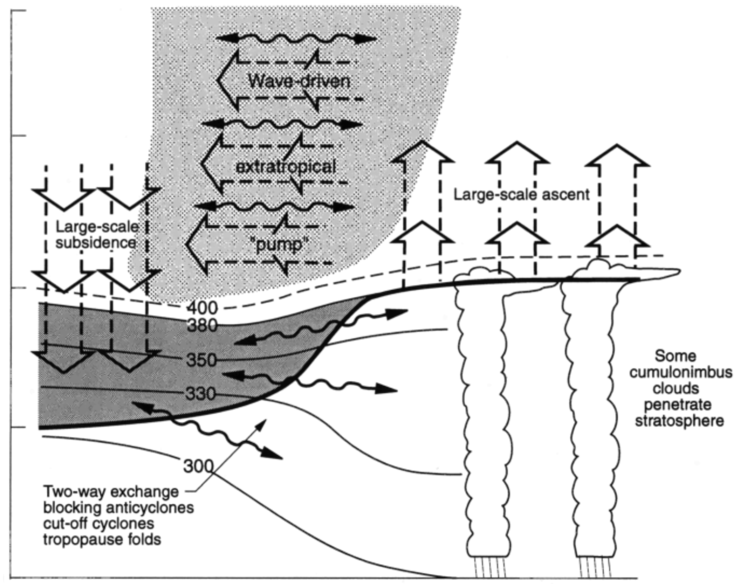

Figure 1.1: STE in the framework of large-scale circulation. The thick line is the tropopause, whereas the thin lines are isentropic surfaces [K]. The heavily shaded area is "lowermost stratosphere", the stratospheric part of the middle world. Taken from Holton et al. (1995), their Figure 3.

3. they merely account for the net flux.

In order to study the STE of tracer species that have strong gradients across the tropopause such as ozone and nitrogen oxides, however, it is essential to understand the geographical and temporal variability of those processes. Therefore it is necessary to consider smaller-scale processes and their associated STE across the tropopause, since global averaged estimates across the 380-K isentropic surface are insufficient. It is noteworthy that these two frames must be closely linked with each other, and the detailed processes ensuring this closure are yet to be clearly understood.

1.4 STE in the context of smaller-scale processes

1.4.1 Synoptic- and meso-scale mechanisms

In the present study the main focus is placed upon the midlatitude STT taking place at the bottom of the middle world defined in Section 1.3. In the midlatitudes and subtropics, several synoptic- and meso-scale processes are known to be responsible for STT: Tropopause folds in the vicinity of jet streams (Danielsen 1968; Vaughan 1988; Ebel et al. 1991), cutoff lows (Vaughan 1988; Price and Vaughan 1992; Ebel et al. 1991), Rossby wave breaking (Lamarque et al. 1996), as well as mesoscale convective complexes (Poulida et al. 1996). Among them, tropopause folds and cutoff lows are thought to be the most significant processes for transport of stratospheric air into the troposphere, being associated with large latitudinal displacements of the tropopause on isentropic surfaces (Stohl et al. 2003). Tropopause folds refer to the formation of elongated filaments of PV contours on isentropic surfaces in regions of upper-level troughs or cut-off lows, whereas cutoff lows are the isolated cyclonic vortices in the upper-level flow. Bithell et al. (1999) in their three-dimensional simulation observed the development of both of those features in the dynamical tropopause during a baroclinic wave life cycle in the Northern Hemisphere.

Cutoff lows form as an extrusion from a tongue of high potential vorticity from the polar stratosphere on an isentropic surface (Vaughan 1988; Price and Vaughan 1993). Due to the necessity to retain the thermal wind balance, the troposphere beneath the cutoff lows can become unstable (Hoskins et al.

1985), so that the vortex induces deep, vigorous convection leading to an efficient mixing between the stratospheric air confined in the system and the tropospheric air below (Ebel et al. 1991). It was confirmed by Bamber et al. (1984) using aircraft measurements of fluorocarbons, hydrocarbons and ozone that convective mixing of stratospheric and tropospheric airs occurs inside such systems, with coherent features lasting for over two weeks. Price and Vaughan (1993), in their statistical study of the size and distribution of cutoff low systems, identified that polar cutoff cyclones, which usually extend to mid-latitude regions, are the only type that play important role in the tropospheric ozone budget.

Tropopause folding, on the other hand, occurs typically in conjunction with baroclinic waves and upper-level frontogenesis in the upper tropospheric polar jet stream region (Beekman et al. 1997) and often forms during the development of a cutoff low (Stohl et al. 2003). Its concept being first introduced by Reed (1955) and Reed and Danielsen (1959), tropopause folding is now known to be the primary mechanism that accounts for the majority of the downward ozone flux (e.g. Reed and Danielsen 1959; Shapiro 1980; Lamarque and Hess 1994; Sprenger et al. 2003). Once such a folding structure is formed, the stratospheric air can descend along isentropic surfaces adiabatically southward and beneath the jet streams (WMO 1986). Irreversible transfer across the tropopause can then be caused by mixing with tropospheric air via turbulence (Shapiro 1980), diffusion (Stohl et al. 2003), and diabatic processes (Danielsen 1968), which can physically destroy the filaments consisting of stratospheric air.

Most of these processes associated with STE are periodic in nature with timescales shorter than the approximately 22 days of free tropospheric photochemical life time of ozone; thus, STE processes can perturb significantly the tropospheric ozone budget (Bourqui and Trépanier 2010).

1.4.2 Numerical modeling

Numerical modeling has been of great interests for numerous studies focusing on STE processes and estimating the ozone budget, especially in light of the spatio-temporal limitations of observations.

The difficulty in modeling the processes associated with STE arises from that, as discussed in Gray (2003) and Bourqui (2006), the resolution has to be high enough so that the involved processes as discussed in Section 1.4.1 as well as the associated flow can be adequately resolved. Bourqui (2006), in their sensitivity test, showed that STT is sensitive especially to the model spatial resolution, and that spatial resolution of at least $1^o \times 1^o$ and the temporal resolution of 1 hour are required in order to capture STE events accurately.

In earlier studies, the Eulerian methodology introduced by Wei (1987) was extensively used in order to diagnose STE. Wirth and Egger (1999), however, found in their study that the reliability of the Wei's method is largely dependent on the vertical coordinate system used in the calculations. By using a case study with a cutoff low system, they conducted an intercomparison of five different methodologies and demonstrated that the Wei's method, with pressure or potential temperature as a vertical coordinate, suffers from an extensive cancellation of several large terms, which leads to appearance of small-scale artificial features. On the other hand, Wei's method using PV as a vertical coordinate as well as the Lagrangian trajectory method proved to give a reasonable STE mass flux estimate without such cancellation and artifacts. Nonetheless, these two methodologies produce different results, as only the Lagrangian trajectory method takes into consideration all non-conservative processes on the resolved scale, such as implicit model diffusion in the advection scheme. Wei's method with PV as a vertical coordinate further requires the knowledge of the PV budget, which is not available from most model outputs. Thus the Lagrangian methods are more robust than the Wei's approach, although a limitation remains as they lack subgrid convection and turbulent mixing (Gray 2003).

1.5 Research motivations

As mentioned earlier, stratospheric ozone is essential in sustaining the cleansing mechanism of the troposphere while it becomes hazardous for human's respiratory system at high surface concentrations. The STT contribution to ozone budget, however, is still heavily debated, with a current estimate being rather wide range of from 25 to 50 % (Bourqui and Trépanier 2010). Furthermore, recent studies have suggested that the tropospheric ozone of the stratospheric origin may increase in response to the expected strengthening of the Brewer-Dobson circulation associated with climate change (e.g. Sudo et al. 2003). Thus, an improved understanding of the STT is needed.

The main goal of the present study is to validate a new STT datasets produced by applying a Lagrangian methodology to the high-resolution global operational forecasts from Environment Canada, with use of measurement profiles taken during an ozonesonde balloon campaign lasting approximately one month during the summer 2010 as a reference. The same methodology has been used in the previous studies (e.g. Wernli and Bourqui 2002; Sprenger and Wernli 2003). They are, however, mainly based on (re-)analysis data. Although these (re-)analysis data are very useful for many purposes, providing best available long-term data on global scale, those data have significant noise which are unavoidably introduced by data assimilation processes (Bourqui and Trépanier 2010). On the other hand, the use of weather forecasts, such as the one used in this study, does not suffer from such noise. A Lagrangian methodology has never been applied to operational forecasts; therefore, the success of this project will enable us to predict STT events daily and provide warnings accordingly, which will be beneficial for many purposes. In addition, it will also help us better understand and quantify STT contributions to the tropospheric ozone budget globally.

The structure of this thesis is as follows: In Chapter 2, the Lagrangian methodology used in this study, the measurement dataset as well as the determination criteria for intrusion levels are described. The results are presented and discussed in Chapter 3, while Chapter 4 provides a discussion on the previous chapter. In Chapter 5, an automatic algorithm is introduced as an alternative method for determining the intrusion levels from a measurement profile and the results are presented. Finally results are summarized and conclusions are drawn in Chapter 6.

Chapter 2

Methodology

2.1 Description of STE forecast data

The new Lagrangian STE diagnostic model has been running operationally at Environment Canada (EC) on the global scale since 8 July, 2010. It is based on hourly outputs of EC Global Environmental Multiscale (GEM) Model global forecasts with the horizontal resolution of $0.3^o \times 0.3^o$ and 90 vertical levels up to 0.1 hPa. See Côté et al. (1998a), (1998b), and Yeh et al. (2002) for more descriptions of the model.

Three-dimensional kinematic trajectories are calculated daily from five forecast times (00 h, 24 h, 48 h, 72 h, and 96 h), starting on a regular grid of 55 km $\times$ 55 km $\times$ 5 hPa in the forward direction for a duration of 6 days, so that each trajectory carries a mass of Δ m = 157×10^9 kg. The 6 day duration was chosen instead of the available duration of 10 days, as hourly outputs are available only for the first 6 days, thereafter increasing to 3-hourly.

In this study, we only consider the trajectories started at the initial time of each daily forecast. 50 million of such trajectories are calculated daily, as well as several physical and dynamical variables along them, including potential vorticity and potential temperature. The trajectory calculation is based on the LAGRangian ANalysis TOol (LAGRANTO) developed by Wernli and Davies (1997), yet the code was greatly modified in order to accommodate various options of trajectory selections and the special format of GEM model outputs. Note however that the scheme does not include turbulence and convection parameterizations as mentioned in Section 1.4.2.

Once the trajectories are calculated, only those that crossed the dynamical tropopause within the time-window [12 h, 36 h[are selected. The dynamical tropopause is defined as either the 2 PVU surface or the 380 K isentropic surface. In this study, we only consider the trajectories crossing the 2 PVU tropopause as the focus is placed on the midlatitudes. This choice of 2 PVU surface for the extratropics turn out to match fairly well with the thermal tropopause taken from the measurements, as will be discussed later.

A residence time criterion is also applied in the trajectory selection procedure following Wernli and Bourqui (2002). Residence time $\tau^{\star}$ is defined as a threshold period of time that each trajectory must reside in either sides of the tropopause, before and after crossing the tropopause. The schematic diagram of this concept is shown in Figure 2-1. Wernli and Bourqui (2002) discussed that some air parcels oscillate between the troposphere and the stratosphere across the tropopause on short timescales (during T^{trans} in Figure 2-1), which intrinsically stems from the spatial smoothing of the dynamical tropopause calculated as a secondary field from the original wind data. These parcels spend only a short time in the other region before flowing back to the original layer, so that they would merely have a negligible chemical impact. Thus the introduction of the residence time criteria ensures to avoid such spurious and insignificant exchange events across the tropopause. The STT net budget is sensitive to the residence time criteria chosen as shown in Bourqui (2006). It was demonstrated that residence time of 8 h or greater successfully removes the majority of such events. In general the greater the residence time the less the exchange mass. In this operational case the residence time of $\tau^\star = 12$ h is used.

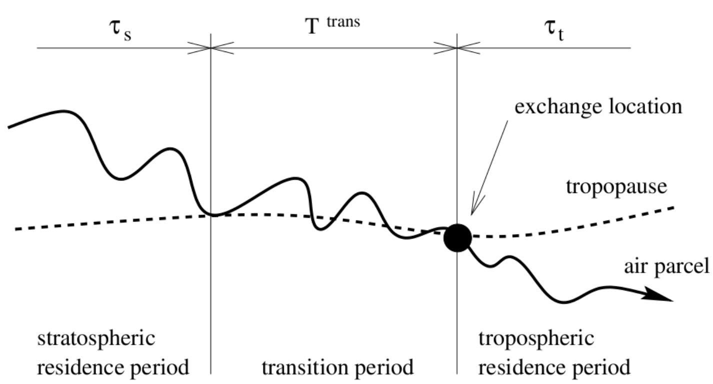

Figure 2.1: Schematic diagram of the residence time criterion applied on a trajectory. If $\tau_s > \tau^\star$, $\tau_t > \tau^\star$, a trajectory is regarded to experience a significant exchange. Excerpted from Bourqui (2006), their Figure 2.

Furthermore, in order to facilitate the analysis of deep stratospheric intrusions, the selected trajectories that penetrate into the troposphere as deeply as 700 hPa are organised into clusters, following Bourqui and Trépanier (2010). A cluster is defined as a set of ten or more trajectories that have a time-averaged distance from each other smaller than a given threshold distance. In the present study, it is set to 222 km, to require the compactness in each cluster during the tropospheric descent. Thus each cluster essentially represents an individual deep STT event, which is defined as when parcels rapidly descend from the tropopause to 700hPa within no more than 5 days (Wernli and Bourqui 2002). Deep intrusion events can significantly perturb the lower tropospheric ozone budget and impact air quality by bringing air of stratospheric origin into the PBL. It was shown that the 70 % of such trajectories reaching 700 hPa belong to clusters, and that most of these clusters remain very compact during their descent until they reach the lower troposphere and then disperse quasi-horizontally (Bourqui and Trépanier 2010).

2.2 Description of measurements

The Lagrangian STE forecasts were used in a recent ozonesonde field campaign in order to predict deep STT events. The measurements taken from the campaign in turn were used to validate the STE forecasts. The campaign took place from 12 July to 4 August 2010, at three launching locations in Canada: Montreal, Quebec (45.3^{o}N 73.4^{o}W), Egbert, Ontario (44.2^{o}N 79.8^{o}W), and Walsingham, Ontario (42.6^{o}N 80.6^{o}W). The author took part in the campaign and took the measurements at Montreal station sponsored by Environment Canada and Canadian Space Agency. At each location a balloon equipped with an ozonesonde and a radiosonde was launched at 1 p.m. local daylight savings time (17 UTC) daily, measuring vertical profiles of air temperature, pressure, ozone partial pressure, wind speed, wind direction and relative humidity. Other than the regular launches, some special launches were conducted whenever deep STT events were forecast. As mentioned in Section 1.1, the ozone has its largest concentration in the high latitude lower stratosphere, thus presumably deep STT events in this region can cause significant chemical and radiative impacts.

For the campaign, Electrochemical cell (ECC) ozonesondes, developed by Komhyr (1969), were used, which are the most common types of ozonesonde. The instrument is made up of three parts: a Teflon pump, an electrochemical cell divided into two half-cells and an electronic interface. The two half-cells mounted are filled with different concentrations of potassium iodide (KI) solutions in the cathode and the anode, each connected with a platinum electrode. The sonde measures the exterior ozone amount by ozone titration via the redox reaction, which occurs when in contact with outside ozone as:

$$2KI + O_3 + H_2O \rightarrow 2KOH + I_2 + O_2. \tag{2.1}$$

During this reaction, two electrons are released for each ozone molecule, which provides a few milliamperes of current to be measured by the interface. By intercomparison of different ozonesondes, Deshler et al. (2008) showed that ECC ozonesonde has a fairly high precision of less than 2 % in general, lowering to around 4 - 5 % in the vicinity of the surface, the tropopause, and regions with large ozone gradients, and it has another known shortcoming in the tropical troposphere, where the background ozone is smallest (Smit et al. 2007). Also failures in the manual preparation procedure can lower the accuracy by another 6 - 13 % (e.g. Thornton and Niazy 1982; Komhyr et al. 1995).

In the present study the main focus is placed on Montreal measurements, since the measurements were the most abundant and thus consistent among the three locations. Only the data from the regular launches will be presented for most cases for simplicity, although interesting results were found from the measurement data of special launches.

2.3 Detection of stratospheric intrusions

In the existing literature, the bottom and the top levels of stratospheric intrusions in ozonesonde profile are determined subjectively with no explicit criteria that can be applied generally to the whole tropospheric depth.

In the present study the *bottom* of the intrusion levels are subjectively determined for each set of measured profiles based on the following criteria which are listed in descending order of priority:

1. Abrupt decrease in humidity with decreasing pressure,
2. Abrupt increase in ozone mixing ratio with decreasing pressure,
3. A local inversion in temperature profile,
4. High value of negative correlation between humidity and ozone.

The *top* of the intrusion levels follow the same criteria as above, but with signs flipped for the first two criteria. The first and second criteria stem from the fact that an air parcel of stratospheric origin has low water vapour content and high ozone content, as mentioned in Section 1.1. The third criterion is due to the quasi-isentropic descent of the stratospheric air. The potential temperature in the atmosphere increases with height, thus as the air descends from the stratosphere along isentropic surfaces it brings down warmer air, which as a consequence appears in measured profiles as a temperature inversion at the onset of stratospheric intrusion. The last criterion is related to the first two criteria. The top and bottom of intrusions were observed to have anomalously large negative values of covariance, as could be expected.

Note that some extent of arbitrariness is unavoidable in the detection of stratospheric intrusions, especially in places where the air of stratospheric origin has mixed with the surrounding tropospheric air. This causes dilution of stratospheric signatures and makes it nontrivial to detect the level of intrusion unambiguously. The fact that the summer is a season when tropospheric air is richer in ozone than in winter (Stohl et al. 2003) could further contribute to the difficulty as well. Note in addition that tropospheric air can also be occasionally very dry especially in the upper troposphere. Therefore it is essential to take into account both the humidity and ozone for determination of the intrusion levels from the sounding data.

Figure 2-2 is an example of measured profiles. The left panel shows the measured vertical profiles of relative humidity, ozone partial pressure, temperature as well as the thermal tropopause. The intrusion levels determined, following the aforementioned criteria, are overlaid. The right panel on the other hand, is the vertical profile of the number of trajectories forecast by the model which fell within 0.5 degree radius of the Montreal station and within $\pm$ 6 hours of the measurement time. The whole depth of the intrusion was captured fairly well by the model in this specific case.

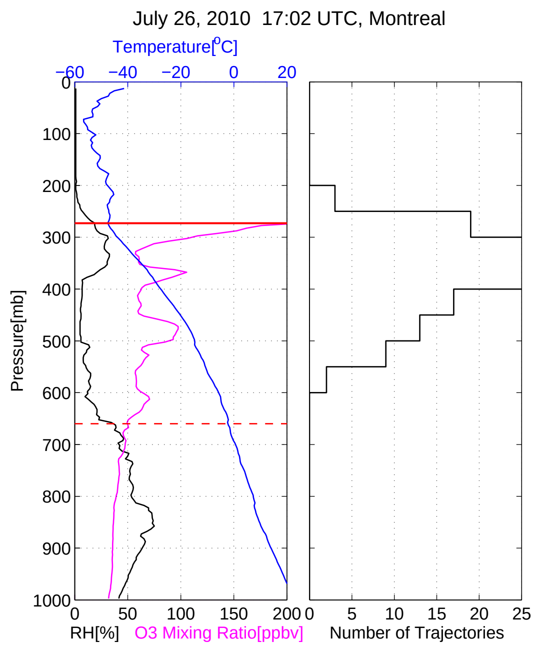

Figure 2.2: Example of measurement vs. forecast profiles on 26 July 2010. Left: Measured vertical profiles of relative humidity [%] (black line), ozone partial pressure [ppbv] (magenta line) and temperature [C^o] (blue line) with intrusion levels (red dashed lines) and thermal tropopause (red solid line) overlaid. Right: The forecast number of trajectories that passed within a 0.5 degree radius of the station within ± 6 h of the measurement time.

Chapter 3

Results

3.1 Overall frequencies of intrusions in observations

The overall frequencies of intrusions in the measurement profiles from the ozonesonde campaign 2010 are summarized in Table 3-1 for each location. The detection method used here is based on the criteria mentioned in Section 2.3. Note that this table is the summary of all the measurements taken, including the special launches.

Location	Measurement	Events(>500mb)	Events(>700mb)
Montreal	25	25	11
Egbert	20	19	11
Walsingham	17	15	4

Table 3.1: Number of intrusions found in measurement profiles for each location during the campaign.

As can be seen from the table, at all three locations there was a very high frequency of STT events, with almost all measured profiles showing intrusions reaching at least 500 hPa. In Montreal and Egbert, approximately as much as one half of the measured profiles show intrusions reaching 700 hPa whereas in Walsingham the fraction drops to approximately one quarter. This is striking given that the summer season, during which the measurement campaign took place, is considered to be the season of minimum occurrence of STT events (e.g. Elbern et al. 1997; Sprenger and Wernli 2003). In comparison, Elbern et al. (1997) found only 195 unambiguous deep intrusion events at one alpine location and 85 cases at another out of a ten-year-long record (all seasons) using the combination of beryllium-7, ozone and humidity, and found lowest STT activities in summer. Stohl et al. (2000) verified their results using measurement data as well as Lagrangian tracer model also for alpine regions, showing that the summer (May to August) has minimum occurrence of STT events of less than 3 %.

Thus our result shown in Table 3.1, where 11 deep STT events were observed within 24 days, is considerably larger than the results in the previous studies. This observed significant difference could possibly be explained by (1) difference in the detection schemes, (2) an increase in STT events potentially due to climate change and/or (3) summer 2010 being an anomalous year for such events. As for (1), both Elbern et al. (1997) and Stohl et al. (2000) utilised beryllium-7 as a primary indicator of the air of the stratospheric origin in order to identify the intrusion as it is produced by cosmic rays above the tropopause and thus one can be sure of its origin unlike the humidity and ozone. Elbern et al. (1997) however showed the coincidence of ozone increase and humidity deficit with increase in beryllium-7, essentially verifying our detection method.

3.2 Comparison of STT forecast with previous modeling studies

Figure 3-1 shows the daily mass flux across 700 hPa which is of stratospheric origin for the domain of $137^o - 23^o$W $\times 33^o - 67^o$N in North America, calculated from the STT forecasts for the period of the measurement campaign. This is to be compared to the values from Bourqui and Trépanier (2010), which is shown in Figure 3-2. In the excerpted figure they displayed the same quantity over the aforementioned domain in North America calculated for four selected days from the trajectory datasets, overlaid on those of Sprenger and Wernli (2003), who showed the climatological median annual cycle of mass flux of stratospheric air through 700 hPa for the period of 1983 - 1993 together with its first and third quartiles. Note that the schemes used in both studies are also based on the Lagrangian trajectory scheme built by Wernli and Davies (1997) but applied to different (re-)analysis datasets.

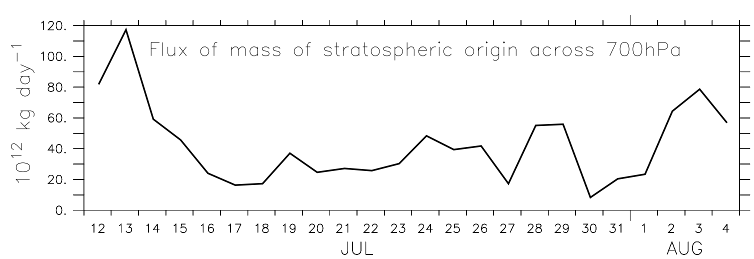

Figure 3.1: The stratospheric-originating mass flux across 700 hPa for the period of the campaign for the domain of $137^o - 23^o$W $\times 33^o - 67^o$N in North America.

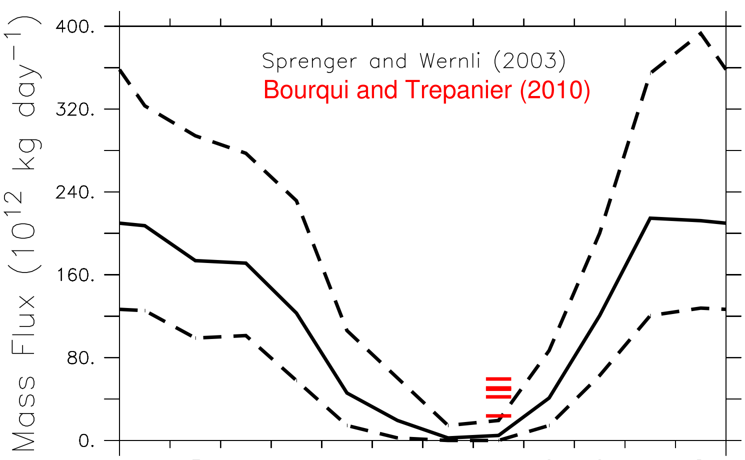

Figure 3.2: Black solid line: Annual cycle of monthly medians of the stratospheric mass flux crossing 700 hPa calculated for the period of 1983 - 1993 from the trajectory datasets of Sprenger and Wernli (2003) in the same domain in North America as Figure 3-1. Black dashed lines: First and third quartiles found in Sprenger and Wernli (2003). Red segments: Stratospheric mass crossing the 700 hPa on four different days in August 2006 in the study of Bourqui and Trépanier (2010).

As can be seen in Figure 3-2, Bourqui and Trépanier (2010) found their daily mass injections to be by an order of magnitude larger than the median found in the study by Sprenger and Wernli (2003) for August, which they identified to be by far the least active time of the year in deep STT events. Our result shown in Figure 3-1 agrees with that of Bourqui and Trépanier (2010), with the maximum mass flux during the period being as much as 120 $\times$ 10^{12} kg per day, well over the third quartile of Sprenger and Wernli (2003) for the season. This in turn confirms the observed large frequency of the stratospheric air ingress into the lower troposphere in summer 2010 as seen in Section 3.1.

Bourqui and Trépanier (2010) suggested three possible factors for their much larger deep STT mass fluxes compared to Sprenger and Wernli (2003): Namely, (1) misrepresentation of the events in Sprenger and Wernli (2003) owing to the low spatio-temporal resolution of the data they based on (1^o horizontal and 6 hour time resolution) compared to the resolution they applied (0.5^o in horizontal and 1 hour in temporal resolution), (2) August 2006 being an anomalously active season in STT events, and/or (3) change in long-term trend in the annual STT cycle potentially as a consequence of climate change. The fact that the present study agreed with their result, however, would likely to eliminate the second possibility, unless both summer 2006 and 2010 happened to be two anomalous summers which observed by far more deep STT events compared to the past 15 years.

One other possibility is the residence time criterion applied in the model for each study. As described in Section 2.1 the residence time of $\tau^\star = 12$ h was used in the present study, whereas in Sprenger and Wernli (2003) a larger residence time of $\tau^\star = 96$ h was used. Bourqui and Trépanier (2010) did not apply any residence criterion in their study as their focus was on deep intrusions only, for which the oscillating exchanges do not come into play. Thus in that sense the condition in Bourqui and Trépanier (2010) is comparable to that of the present study. Residence time of 96 hours used by Sprenger and Wernli (2003) after crossing the tropopause (τ_t in Figure 2-1) is unlikely to account for the resulting discrepancy, since it is very rare for trajectories to go back to the tropopause after having descended down to 700 hPa. The residence time before crossing the tropopause (τ_s in Figure 2-1), however, could be a source of the observed difference. As mentioned in Section 2.1, Bourqui (2006) showed that the application of the residence time of $\tau^\star > 8$ h successfully removes the majority of the spurious events, and with a longer residence time the number of the events decreases slowly. Thus applying $\tau^\star = 96$ h could result in less exchange compared to the case with $\tau^\star = 12$ h as much as by a factor of 2, but it is not likely to be accountable for the tenfold increase seen in the present and the previous studies; thus further investigation is required on this point.

3.3 Selected measured profiles and corresponding STT forecasts

Figure 3-3 and 3-4 show the measurement profiles and the corresponding number of STT forecast trajectories that came within a 55 km radius of the Montreal station within ± 6 h of the measurement time for four cases selected for their representativeness. The selection is meant to show typical combinations of clear/unclear intrusions with good/poor forecasts. Note that each bin in the vertical profile of STT forecasts is 50 hPa.

On 26 July (Figure 3-3 left column, first row. See also Figure 3-1), a clear sign of intrusion was seen in the measurement profiles from 650 hPa to 350 hPa, and was correctly forecast by the model with a vertical error smaller than 100 hPa. On the upper level trajectory chart (second row) it is clear that a dense number of trajectories passed over the station following a northwesterly and westerly flow, with some trajectories intruding below 500 hPa as shown on the lowest panel. A few trajectories at the height of 500 to 600 hPa came right over the station, which accounts for the successful capture of the bottom of the intrusion as seen in the measurement profile.

On 30 July (Figure 3-3, right column), there was a clear sign of intrusion in the observation for the layer between 800 hPa and 300 hPa, yet the model did not capture the lower part of the event but forecast only up to 500 hPa level. Trajectories with pressure levels of approximately 700 hPa, however, appear to have approached very close to the station approximately at 200 km away. These trajectories are part of seemingly clustered structure, which originates from the northwest side of the station and takes a cyclonic path to reach the south/southwest of the station, as shown on the bottom panel.

On 13 July (Figure 3-4, left column) a weak sign of intrusion was observed, without a significant decrease in relative humidity nor increase in ozone observed, from 580 hPa to 410 hPa as well as between 280 hPa and above. Although it was not a marked intrusion, possibly due to some occurrences of mixing and/or the presence of some clouds, the model captured the double intrusion structure fairly correctly. This can be clearly seen in the second and the third rows. In the upper air chart (second row) although most dense struc-

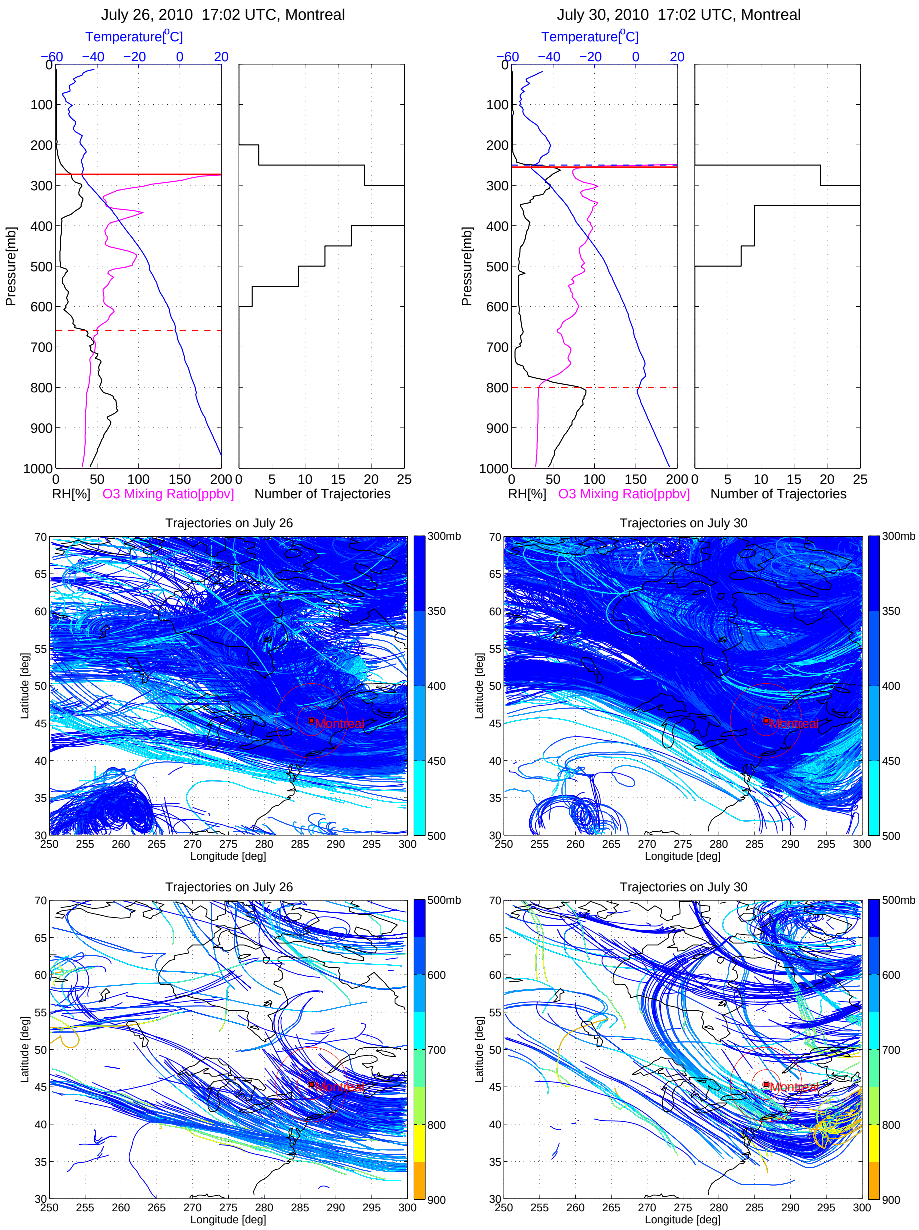

Figure 3.3: For each column, top left panel shows the measured profile of relative humidity [%], ozone partial pressure [ppbv] and temperature [^oC] with bottom and top of intrusion levels as well as the thermal tropopause are overlayed with red dashed lines, blue dashed lines, and solid red lines, respectively, while top right panel shows the forecast number of trajectories that passed within a 0.5 deg radius of the station within ± 6 h of the measurement time. The second and third row show the corresponding trajectory maps for 300 - 500 mb levels and for 500 - 900 mb levels respectively, whose pressure levels are expressed in different colours. The circles represent 5, 3, 2, 1, and 0.5 degree radii of Montreal. The left column shows an example from 26 July, whereas the right from 30 July 2010.

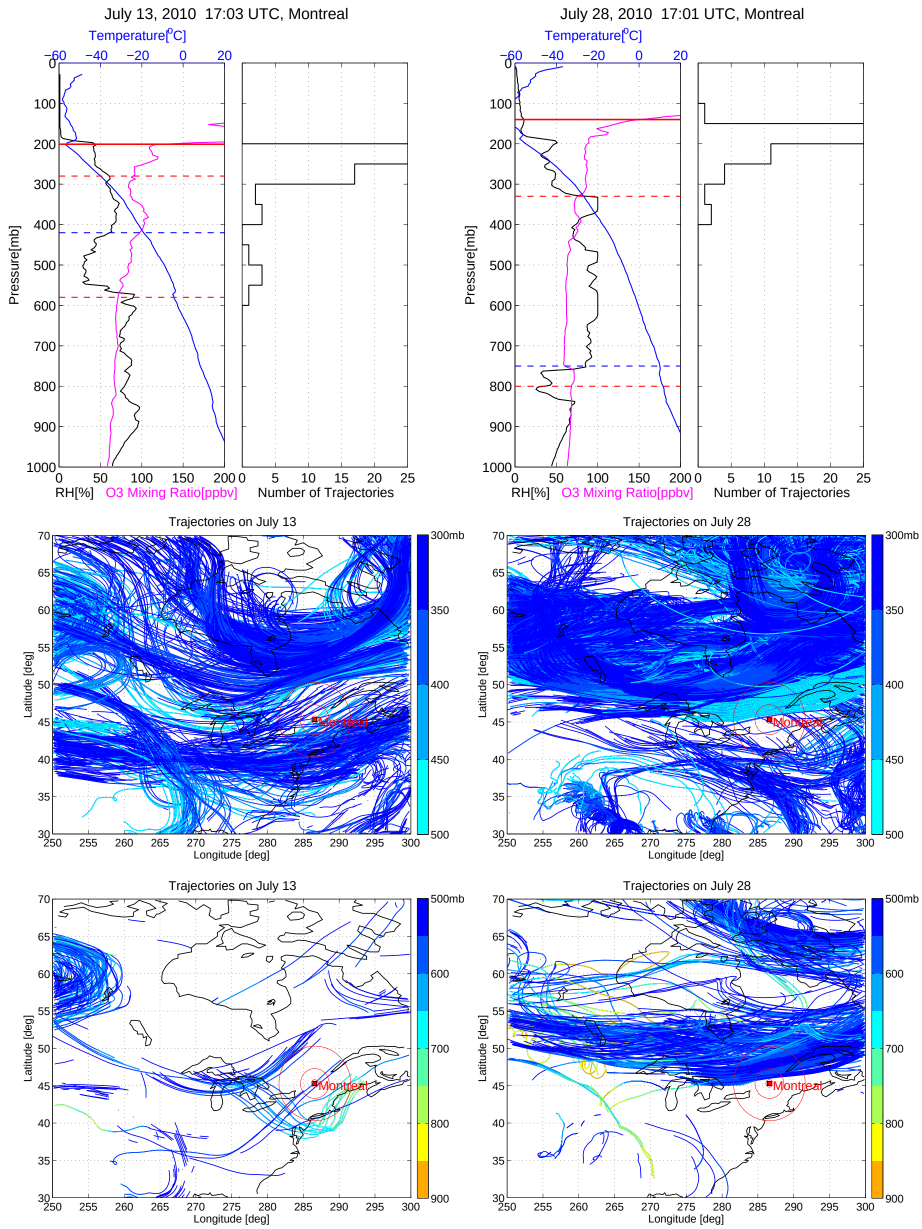

Figure 3.4: Same as Figure 3.3, but for 13 July (left column), and the fourth from 28 July 2010 (right column).

tures of trajectories pass either north or south of the Montreal station, a few come right on top of it. The same structures of trajectories, but sparser, are observed on the third panel as well around 500 - 600 hPa, coming right within the 0.5 degree radius of the station in the vicinity of the inflection point of their pathway.

On 28 July (Figure 3-4, right column), the signature of intrusions in the measurement profile was subtle compared to clear cases. Intrusion levels were identified between 750 and 800 hPa as well as above 330 hPa. The lower intrusion was especially elusive with only slight features of the stratospheric air ingress. As shown on the middle panel, the model captured the upper level intrusion around 300 - 400 hPa, but missed the lower level intrusion from 800 hPa to 750 hPa with no trajectory found at these pressure levels in an extended window around Montreal, unlike the case of 30 July.

3.4 Comparison between observations and STT forecasts

Figure 3-5 (a) exhibits daily measurements of relative humidity [%] in function of pressure levels with each bin representing 10 hPa in the vertical and $\pm$ 6 h of the measurement time (approximately 17 UTC). Figure 3-5 (b) is similar to (a) but for ozone partial pressure (ppbv). The blank columns are where the data are missing due to instrumental failures while the solid black lines are the thermal tropopause height derived from observations. The overlaid black hatched areas are the intrusion levels determined subjectively from the observations.

The corresponding trajectories from STT forecasts that passed over the station within 0.5 degree radius around it within ± 6 h of the regular measurement time for each day is shown in Figure 3-5 (c). The bin size is 50 hPa in the vertical. The hatched areas are again the subjectively determined intrusion levels (with the vertical bin size of 10 hPa). Note that the top edge of the coloured bins in (c) indicates the dynamical tropopause in the model, which matches fairly well with the thermal tropopause levels indicated by the solid black line, confirming that the choice of the dynamical tropopause of 2 PVU surface following Holton et al. (1995) was a fair choice for the extratropics.

The relative humidity and ozone figures clearly show the remarkably high frequency of observed intrusions, with three distinct periods of deep intrusions: Approximately 14 - 20 July, 24 - 27 July, and 29 July - 1 August 2010. Each of these periods seems to last for several days, which roughly corresponds to the baroclinic life cycle time-scale, suggesting the association with baroclinic disturbances as described in Bourqui and Trépanier (2010). A similar overall structure can be seen in the trajectory plot with a good capture of events down to 500 hPa, but with events below 500 hPa underestimated. The inner side of the white contours in Figure 3-5 (a) and (b) denotes forecast trajectories with ages less than 60 h. Bourqui and Trépanier (2010) showed that trajectories retain a high degree of compactness, with typically 80 % of their stratospheric compositions conserved, while the air descends along isentropes, until the quasi-horizontal dispersion phase starts usually 60 h or later after the descent started. Hence, the areas encircled by the white contours correspond to the areas with expected high ozone and low humidity contents. While the

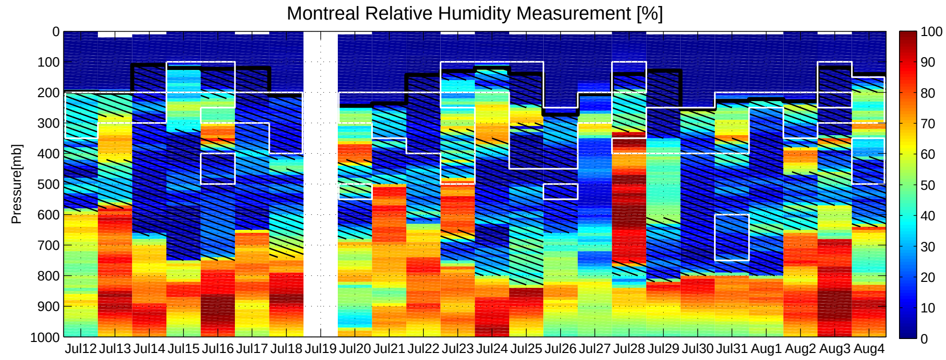

(a)

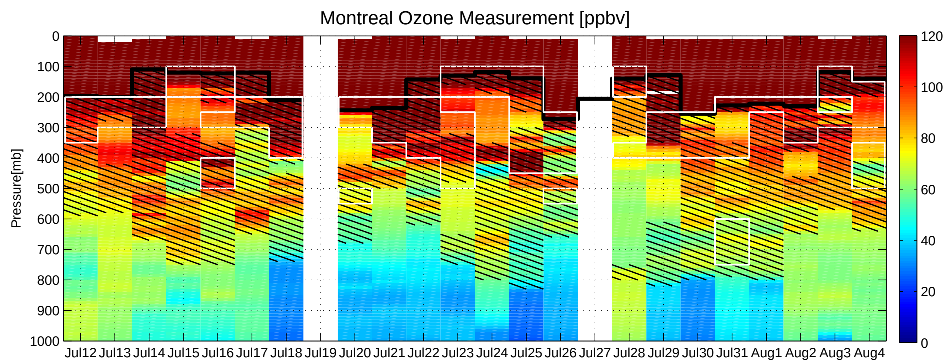

(b)

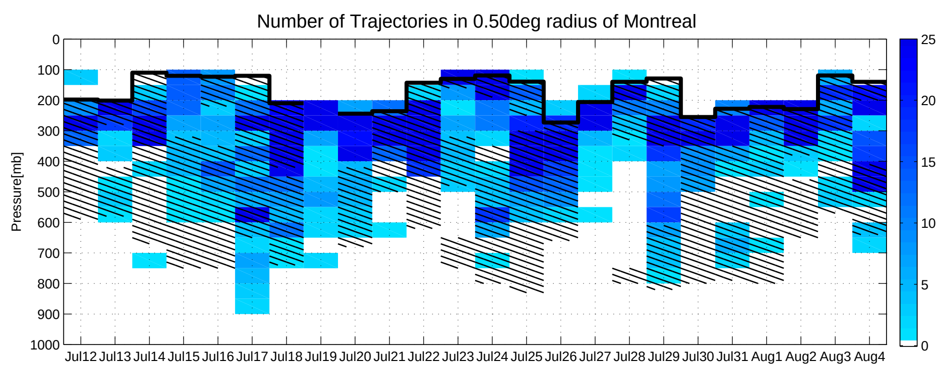

(c)

Figure 3.5: 2D histograms for daily measurements at Montreal station of (a) relative humidity, (b) ozone partial pressure, and (c) corresponding number of forecast trajectories incoming within 55 km of Montreal with bins of 50 hPa $\times$ 12 h. The solid black lines are the measured thermal tropopauses, whereas the white contours in (a) and (b) indicate where the corresponding forecast trajectory ages are less than 60 h. The hatched areas are the subjectively-determined intrusion levels. The blank columns in (a) and (b) are where data are missing.

match is not perfect, some degrees of correspondence is evident in Figure 3-5 (a) and (b).

In order to provide an overall measure of the comparison between model and observations, the fraction of missed events was calculated as follows:

$$\text{Percentage of missed events [\%]} = 100\% \times \frac{N_P^{missed}}{N_P^{captured} + N_P^{missed}}$$

and similarly, the percentage of overforecast by the model was calculated as follows:

$$\text{Percentage of overforecasts [\%]} = 100\% \times \frac{N_P^{overforecast}}{N_P^{captured} + N_P^{missed}}$$

where N_P^{missed}, $N_P^{captured}$, and $N_P^{overforecast}$ are the number of missed events, events correctly forecast, and overforecast by the model within each pressure level as listed below, respectively. The overall percentages of missed events in function of pressure levels are found to be:

- $300hPa \leq P < 500hPa : 16.1\%$
- $500hPa \leq P < 700hPa : 48.3\%$
- $700hPa \leq P < 1000hPa : 73.1\%$,

whereas the percentages of overforecast by the model yield the following:

- $300hPa \leq P < 500hPa : 29.2\%$
- $500hPa \leq P < 700hPa : 8.4\%$
- $700hPa \leq P < 1000hPa : 25.0\%$.

Thus overall, the forecasts are fairly reliable in the upper troposphere above 500 hPa with slight overestimation, yet the skill progressively deteriorates towards the lower troposphere and statistically speaking, there is a net underestimation of 50 % below 700 hPa. This result has an important implication to the stratospheric mass fluxes across 700 hPa shown in Section 3.2. The fact that about one half of the events that ingress below 700 hPa were missed would virtually imply that the mass flux shown in Figure 3-1 must be doubled in order to match better with the observed stratospheric intrusion, which would result in tremendous mass exchange, even more deviating from the values estimated by Sprenger and Wernli (2003).

3.5 Towards the validation of the model

In order to investigate the model output against measurement data in more detail, each vertical 50 hPa bin in individual measurement was assigned one of the following categories based on the subjectively detected intrusion levels (black hatched areas in Figure 3-5): *Above Intrusion*, *Intermediate*(*top*), *Inside Intrusion*, *Intermediate*(*bottom*), and *Below Intrusion*. The *Intermediate*(*top*) and *Intermediate*(*bottom*) layers are defined as the best centred 100 hPa bin covering the identified tops and bottoms, respectively. The air in this category can be thought as intermediate between tropospheric and stratospheric compositions, depending on the local mixing activity. In case there exist multiple intrusion layers in a measurement profile with less than 100 hPa distance between the two consecutive layers, the *Intermediate*(*top*) of the lower intrusion is overwritten with *Intermediate*(*bottom*) of the upper one. If there lies more than 100 hPa in between, 100 hPa closest to the top of the intrusion level of the lower intrusion layer are marked as *Intermediate*(*top*), 100 hPa closest to the bottom of the intrusion level of the upper intrusion layer are designated the *Intermediate*(*bottom*) class, whereas the layer in between, if any, is assigned the category of *Above Intrusion*. Note that the value of 100 hPa was arbitrarily determined. An example is shown in Figure 3-6, which shows a case when two intrusion levels exist with more than 100 hPa distance in between.

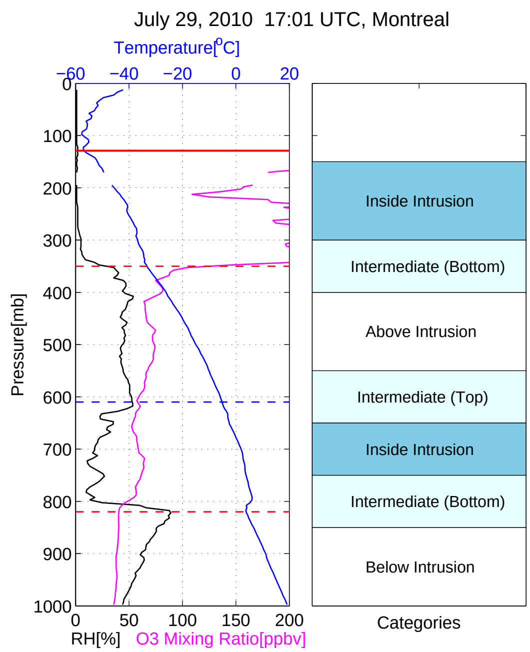

Figure 3.6: Example of measurement and the corresponding vertical profile of subjectively-determined categories on 29 July 2010. Left: Measured vertical profiles of relative humidity [%] (black line), ozone partial pressure [ppbv] (magenta line) and temperature [C^o] (blue line) with bottom and top of intrusion levels (red and blue dashed lines, respectively) and thermal tropopause (red solid line) overlaid. Right: The categories assigned for each vertical 50 hPa level which are subjectively determined based on the measurement shown on the left.

The number of 50 hPa bins through all measurement profiles taken at

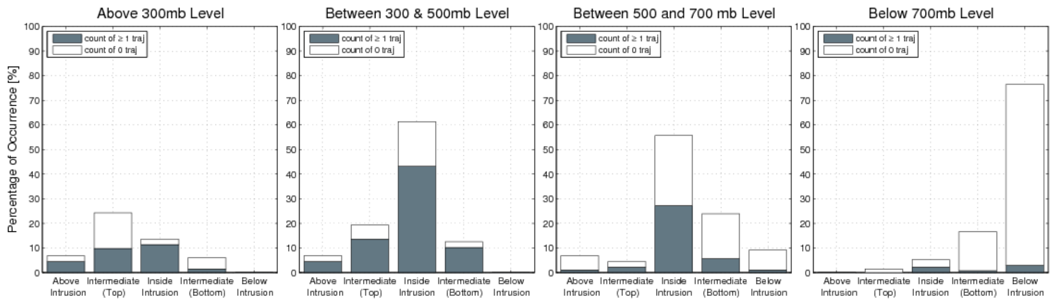

Figure 3.7: The sum of the counts of either zero or one (or more) trajectory forecast in 50 hPa bins for the subjectively-determined categories: Above intrusion, intermediate (top), inside of the intrusion, intermediate (bottom), and below intrusion. The four columns show different pressure regions. Vertical axis is normalised with respect to the total number of 50 hPa bins in a given pressure region through the profiles. The white coloured bars are the counts of zero trajectory, while the gray bars are the counts of one or more trajectories.

the Montreal station are counted as a function of the category and plotted in Figures 3-7 and 3-8. The statistics are made separately for $<$ 300 hPa, 300 - 500 hPa, 500 - 700 hPa and $>$ 700 hPa, and are normalised to the total number of 50 hPa bins observed at the corresponding pressure levels above the station. Note that the fractions in the above 300 hPa level do not add up exactly to 100 % as the trajectories above the thermal tropopause were omitted.

Figure 3-7 shows the presence of trajectory forecast by the STT model (either zero, or one or more trajectories) found in each corresponding 50 hPa bin. Counts of one or more trajectories found in the category *Inside Intrusion* can be interpreted as a correct model forecast. Counts of zero trajectory in this category represent events missed by the model. Counts of one or more trajectories in the categories of *Above* and *Below Intrusion*, on the other hand, implies an overforecast by the model. As can be seen in Figure 3-7, there are a lot of trajectories reaching at between 300 hPa and 500 hPa level (second

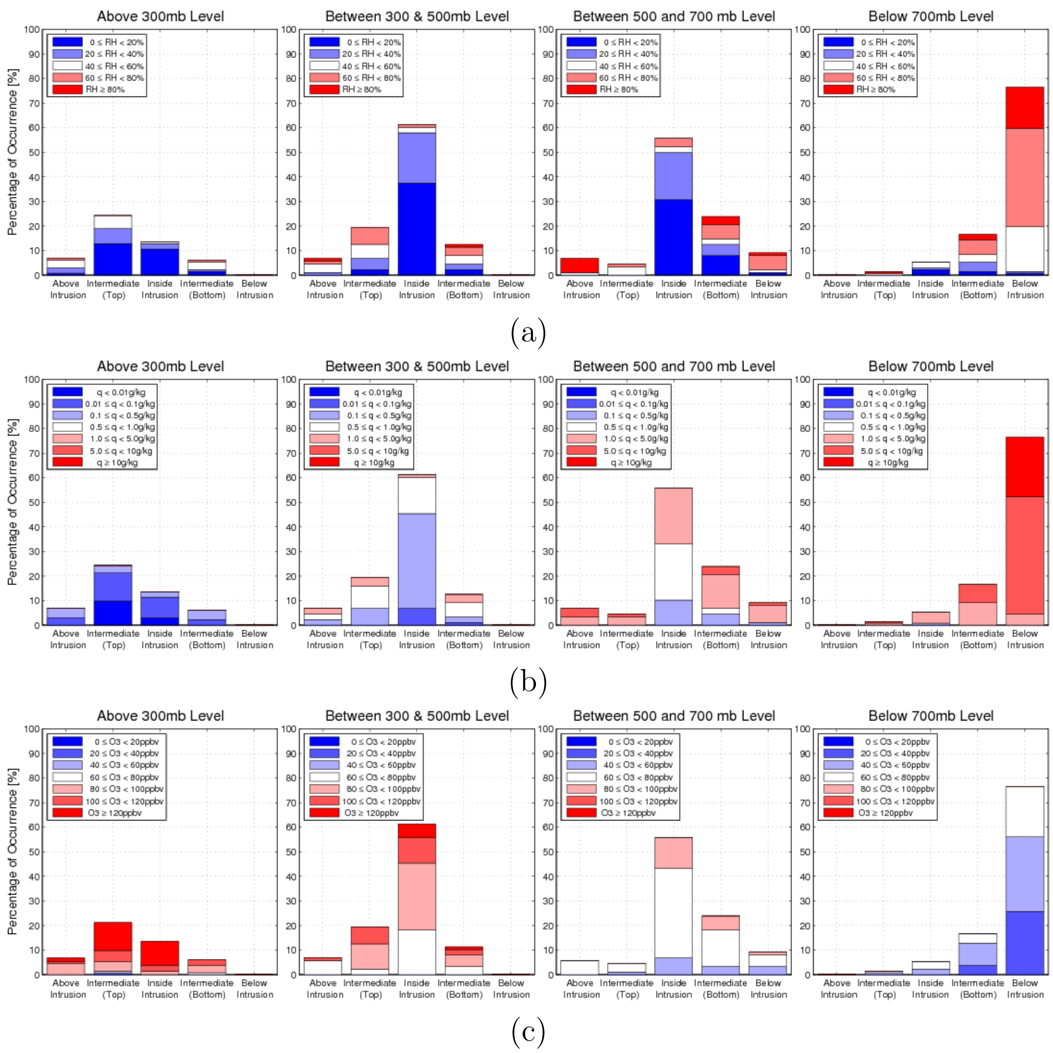

Figure 3.8: (a) The distribution of relative humidity [%] for each pressure region and category of the subjectively-determined intrusion levels. (b) Same as (a) but for specific humidity [g/kg]. (c) Same as (a) and (b) but for ozone mixing ratio [ppbv].

column) and between 500 hPa and 700 hPa (third column), but below 700 hPa the number of intrusions falls to very small frequencies, suggesting that the PBL prevents stratospheric intrusions from penetrating lower down, or removes stratospheric signatures by intense mixing. It is also noticeable that the forecast skills gradually drop with increasing pressure as noted earlier, with majority of the events captured above 500 hPa, and below that the accuracy decreasing to about one half. When focusing on the *Above* and *Below Intrusion* categories, it is clear that the majority of the overforecast comes from above 500 hPa.

Figure 3-8 (a) shows the distribution of relative humidity [%] for each category for the four pressure regions. Fairly clear stratospheric signatures of low humidity can be seen in the *Inside Intrusion* category at all pressure regions, whereas *Above* and *Below Intrusion* categories display more tropospheric distributions with *Intermediate* (*top*) and (*bottom*) lying in between, as anticipated. Interestingly, the range of relative humidity values within the intrusion levels seem to be rather independent of the height levels, seemingly suggesting the very high degree of retainment of this stratospheric signature even deep in the lower troposphere. This feature however has to be dealt with caution, since the relative humidity has a dependence on the temperature, as can be seen in its formula:

$$RH = 100 \times \frac{W_s(\text{at temperature T}_d \text{ and pressure P})}{W_s(\text{at temperature T and pressure P})}, \tag{3.1}$$

where W_s is the saturation mixing ratio which depends on air temperature and pressure, and T_d is the dew point temperature.

In order to elucidate the ambiguity arising from the use of relative humidity, corresponding distributions of specific humidity [g/kg] are shown in Figure 3-8 (b). It is evident that the specific humidity behaves very differently from the relative humidity, exhibiting more variations in function of pressure levels for all categories of intrusion levels and becoming increasingly moist with increase in pressure. *Inside Intrusion* categories still show more of a stratospheric signature compared to *Intermediate* and the *Above* and *Below Intrusion* throughout all the pressure levels; however, the relative difference among different categories is weaker compared to the relative humidity distributions. Note that the colour scheme is not linear for the specific humidity. Figure 3-8 (c) on the other hand is the same as (a) and (b) but with ozone partial pressure [ppbv]. The ozone distributions reveal similar patterns as in specific humidity, shifting progressively from stratospheric to more tropospheric signatures deeper in the troposphere. This is clearly indicating the diminishment of the stratospheric signatures as the air descends, suggesting the progressive mixing with tropospheric air. The combination of the Figure 3-8 (b) and (c) hints that the observed weakening of the ozone mixing ratio is solely due to the mixing of the air with the surrounding tropospheric air, and not through the occurrence of photochemical processes.

3.6 Cluster analysis for the missed events

To understand the causes of the missed events seen in Section 3.4, clusters of trajectories reaching 700 hPa formed as in Section 2.1 are analyzed. Table 3-2 summarizes the details of the clusters which approached the Montreal station within 10 degree radius for each day when the intrusion event was missed by the model, indicating the associated number of trajectories. Note that the clusters with label (ex) are those which would have reached the station if they were slightly extended in time.

Date	Bottom of intrusion level [mb]	Number of trajectories per cluster (label)
July 12	580	26, 25
July 15	740	195(Fig.3-9), 86(ex)(Fig.3-13), 27
July 16	720	296(D), 195, 172(D), 87(ex), 57, 50, 27, 26(Fig.3-10), 13(ex), 11(ex)(Fig.3-14), 10
July 22	620	none
July 23	700-750	14
July 25	830	46(D), 32, 24(ex), 13
July 28	800-750	84(ex), 13
July 30	800	104, 67, 41(D)(Fig.3-11), 29
August 1	800	129(D), 75(D), 40, 16(Fig.3-12)
August 2	760	129(D), 75(D), 40, 16
August 3	670	129(D), 75(D), 40

Table 3.2: List of candidate clusters for each day when events were missed by more than 100 hPa by the STT forecasts. The intrusion levels shown here are the ones determined subjectively and the levels are meant to be either the lowest intrusion levels or a thin layer of stratospheric air ingress missed by the forecasts. Each cluster is expressed with its number of trajectories, and some clusters are counted multiple times over a few days as potential candidates for missed events. The labeled clusters are shown in Figure 3-9 - 3-14 for further discussion. The label (ex) denotes clusters that could have reached the station if they were slightly extended beyond the six day period.

As can be seen in the table, except for 22 July there appear to be multiple clusters in the vicinity of the station being located at the accurate pressure levels. This implies that for the vast majority of the missed events, geographical shifts can account for the missed forecasts.

3.6.1 Closer look at individual clusters for selected cases

In order to investigate the clusters in more detail, each cluster is plotted from four different spatio-temporal aspects, with four best candidates among them as indicated by labels from Figs. 3-9 to 3-12 in Table 3-2. Here only four selected cases were presented, but the rest of the listed clusters follow more or less similar patterns.

The cluster displayed in Figure 3-9, containing 195 trajectories (mass of 31×10^{12} kg), originates from the region of Arctic Archipelago and descends southeastward rather quickly from around 400 hPa down to 800 hPa within a few days. The observed event on 15 July 2010, 2 days after the cluster started, was detected down to 740 hPa. The cluster approached fairly close to the station around the designated time in a range of height from 450 hPa to 750 hPa, yet shifted to the east of Montreal. Until then the structure remained quite compact, while on its third day it experienced some horizontal dispersion turning in a cyclonic manner and moved over the Atlantic.

The cluster shown in Figure 3-10 is a rather small cluster containing only 26 trajectories (mass of 41×10^{11} kg). After it started on 11 July, it followed the westerly flow slowly advancing eastward and downward, till it reached the closest point to the station on day 5 (the time the event was observed), slightly shifted northward. As can be seen from the figure showing the horizontal distance to the station against time elapsed, at one point the cluster was located within a few degrees of Montreal except for two trajectories which deviated from the main pathway from day 4. The seemingly compact structure on the horizontal view as shown on the fourth panel however started to diverge vertically from day 4, and by day 5 when the cluster came closest to the station, it was spread vertically in a range from 600 hPa to 850 hPa, within which the detected lowest pressure level of 720 hPa falls.

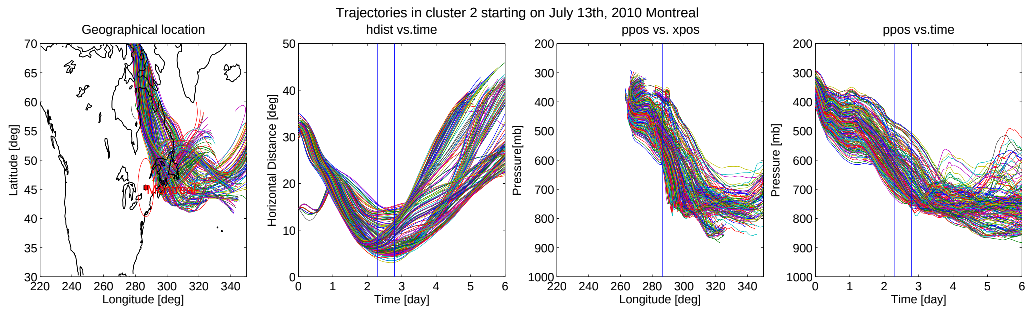

Figure 3.9: A selected case of cluster candidates for missed events, starting on 13 July 2010 to account for the missed event on 15 July 2010, as indicated in Table 3-2. The leftmost panel shows the two-dimensional geographical location of the cluster (latitude × longitude [deg]), the second panel shows the horizontal distance from the Montreal station [deg] against time elapsed [days] after the cluster calculation started, the third panel shows that on the pressure [mb] vs. longitude [deg] field, and the rightmost panel shows the pressure [mb] against the time elapsed [days]. The blue vertical lines in the third panel denotes the longitude of Montreal station, whereas those in the second from the left and the rightmost panels show the temporal window of ± 6 hour of the measurement, the criteria applied in order to determine the captured events. The circle around Montreal indicates 5 degree radius of the station.

The cluster shown in Figure 3-11 on the other hand is a case where the trajectories are slightly dispersed and for that reason only, miss Montreal. This cluster, starting on 25 July and containing 41 trajectories (mass of 64×10^{11} kg), took a similar path as the cluster shown in Figure 3-9, originating from Northern Canada and streaming southward while gently turning cyclonically around the station. The structure remained fairly compact until day 5, after which a majority of the trajectories within the cluster kept flowing southward, passing the west edge of 5 degree radius of the station, while a few trajectories

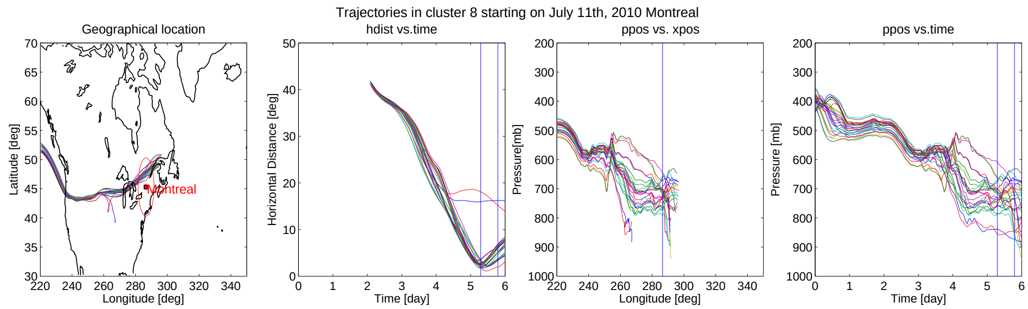

Figure 3.10: Same as Figure 3-9, but for a cluster starting on 11 July for the event on 16 July.

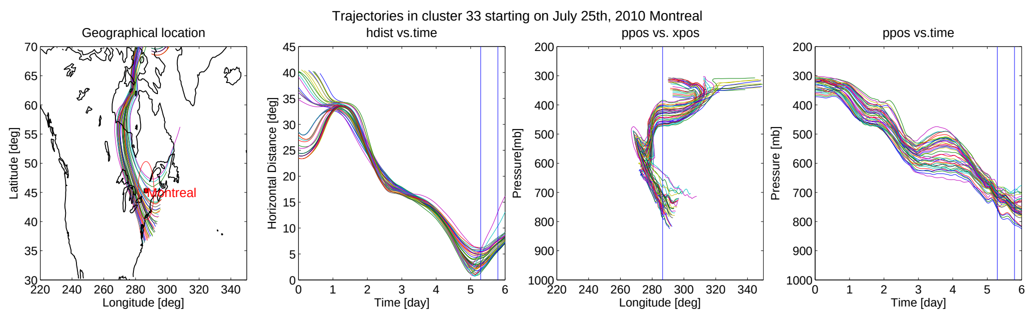

Figure 3.11: Same as Figure 3-9, but for a cluster starting on 25 July for the event on 30 July.

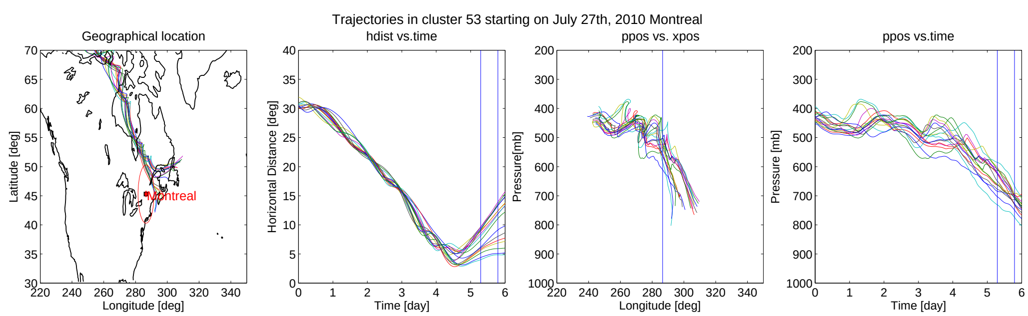

Figure 3.12: Same as Figure 3-9, but for a cluster starting from 27 July, for the event on 1 August.

separated themselves and passed the vicinity of the east edge of the 5 degree radius while quickly turning cyclonically. The observed intrusion level on 30 July, 5 days after the cluster started, was found between 750 hPa and 800 hPa, while the pressure levels of the cluster extended relatively narrow range of from 700 hPa to 800 hPa.

Lastly the cluster presented in Figure 3-12, which comprised of only 16 trajectories (mass of 25×10^{11} kg), also started from Northern Canada from 27 July. On its way south towards Montreal, the cluster descended slowly until day 4 and after that it speeded up to come down to approximately 800 hPa, while wiggling horizontally and vertically. Starting in the middle of day 4 several trajectories deviated towards the east into the Gulf of St. Lawrence while the rest remained in their southward path passing just east of the Montreal station, with pressure levels remaining similar for the two branches from then on. The lowest intrusion level determined on this day was 800 hPa, coinciding the range of the pressure levels of between 600 hPa and 800 hPa the cluster was located at the time, as seen on the rightmost panel.

Thus the above four cases clearly show that the clusters could account for the missed events if they were shifted by only a few degrees. Figures 3-13 and 3-14 as labeled in Table 3-2 on the other hand shows two examples of clusters which a time extension could account for the missed events (see labels (ex) in Table 3-2). The rest of the clusters with label (ex) also follow relatively similar patterns.

The cluster shown in Figure 3-13 started on 9 July from the vicinity of Victoria Island and maintained its compactness until day 2 as can be seen on the second panel. Then, it branched out into mainly three subclusters: The

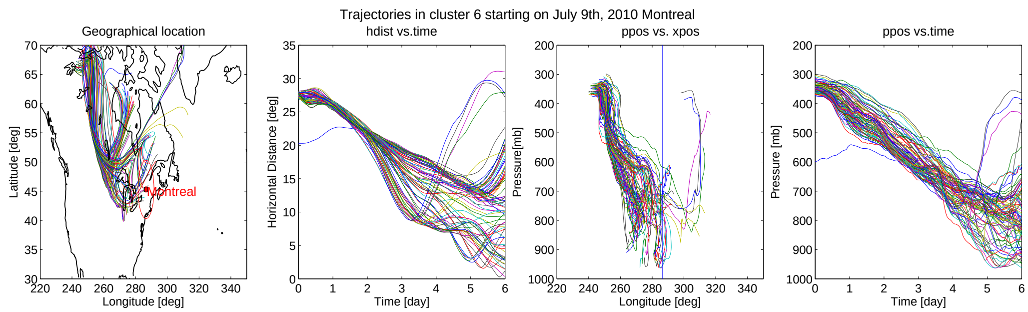

Figure 3.13: Same as Figure 3-9, but for an example of a cluster starting on 9 July that could have reached Montreal with a time extension and accounted for the missed event on 15 July.

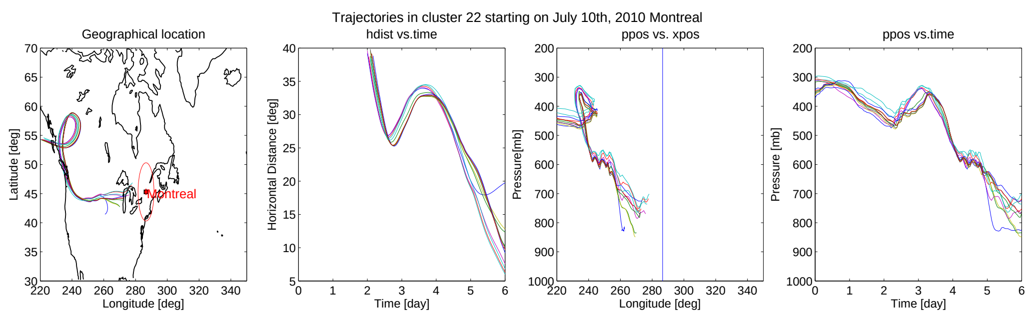

Figure 3.14: Same as Figure 3-13, but for a cluster starting on 11 July that could account for the event on 16 July.

one making an abrupt turn back to the North, the one moderately turning cyclonically and abruptly turning anticyclonically south of Hudson Bay towards Montreal, and the other coming all the way to the Lake Michigan and turning cyclonically towards Montreal. Two trajectories within the third group reached over the Montreal station late on the day 5. For the targeted day of 15 July, or day 6, however, several trajectories seemed to be approaching the station at the pressure level from 600 to 950 hPa compared to the detected level of 720 hPa (the ones at 350 to 450 hPa levels are the ones that went up all the way to Greenland), but due to the cutoff time of 6 days they could not make it to the station.

The cluster in Figure 3-14 started on 10 July in the south of Alaska and advanced quickly its way out to the south while turning cyclonically and then eastward. This fairly small cluster, which consists of 11 trajectories, approached towards the Montreal station retaining its compactness throughout except for one trajectory that deviated from the main path on the day 5 to the south. The main path arrived at Lake Michigan at the end of the six day journey on 15 July at the pressure level of from 700 to 850 hPa, within which the detected intrusion level on 16 July of 720 hPa falls. Given its quick approach to Montreal of 25 degrees within 2 days (the second panel) the cluster could have reached there with an extension of one more day.

As mentioned earlier, trajectories were calculated for 6 days to avoid degradation due to the time resolution of trajectories which decreases after 6 days from hourly to three-hourly. The rapid increase of the GEM forecast errors with time and the chaotic dispersion is expected to further deteriorate the accuracy of trajectories. It is unfortunately impossible to calculate posteriori extensions to these trajectories because the meteorological data are not archived with sufficient time-resolution for reasonable accuracy.

3.6.2 Analysis on the shifted directions of the clusters

In order to investigate potential systematic tendencies in the shifts of the clusters in the missed events listed in Table 3-2, trajectories which fall within 10 degree latitude of the station within $\pm$ 6 hours of the measurement time and within $\pm$ 100 hPa of the detected lowest intrusion level were taken and their average paths were calculated for each cluster. For those clusters with label (ex) which potentially could have reached Montreal with longer duration of calculation, the time range of the last 12 hours was used instead of the former specification. Then the direction of the average path of each cluster with respect to the Montreal station was calculated every hour and represented in the form of a wind rose diagram. Figure 3-15 shows the results with all clusters listed in Table 3-2 except those labeled (ex), while Figure 3-16 shows only with those labeled as (ex).

As can be seen from Figure 3-15, the clusters are found in various directions from Montreal, but the majority of them are situated in the east half, especially between the east-northeast and the east-southeast directions (from 45^o to 135^o meteorological direction), where three dominant directions gather and make up of approximately 40 % of all the clusters considered. In contrast, in the southwest, only a few percent of clusters are found. In terms of proximity, the majority of clusters which were located within 2 degree latitude radius of Montreal appear to be between the east and the south (from 75^o to

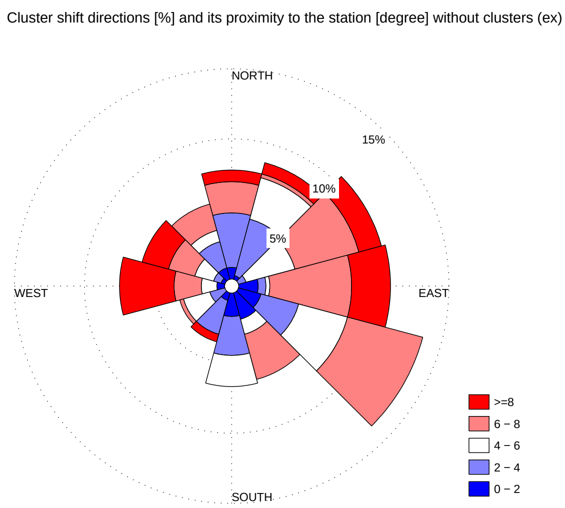

Figure 3.15: Rose diagram of the directions and the distance of the clusters listed in Table 3-2 with respect to the location of the Montreal station except for those labeled as (ex). For each cluster the trajectories which advanced within 10 degree latitude radius of the station within the time range of $\pm$ 6 hours and within $\pm$ 100 hPa of the lowest intrusion level detected were selected and their average distance and the direction with respect to the station was calculated. The percentage of clusters shifted in each direction is indicated by individual cones, while the distribution of the distance to Montreal is indicated by the colours [units of degree latitude].

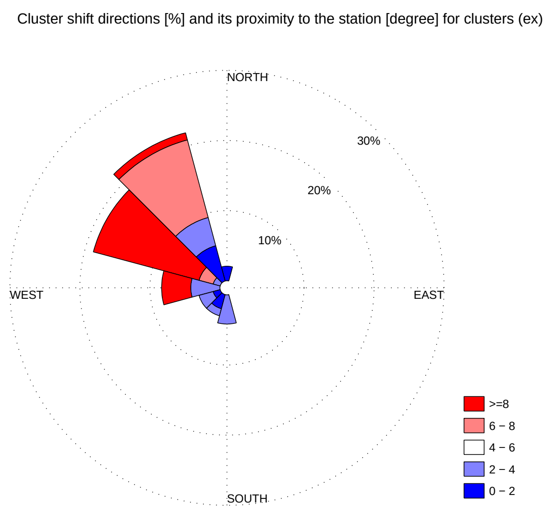

Figure 3.16: Same as Figure 3-15 but for the clusters labeled as (ex) in Table 3-2. The last 12 hours of trajectories were used instead of the temporal criterion used in Figure 3-15.

195^o meteorological direction), whereas those that were located farther than 8 degree radius away with respect to the station are found mainly in two directions: The west and the east. Thus there seems to exist a systematic tendency in the days of missed forecasts to find clusters at the observed altitude but by a few degrees east of Montreal.

On the other hand, the clusters which could have reached the station with calculation longer by a few more days offer a completely different picture, as displayed in Figure 3-16. It is striking that no cluster was found in the east half, but the majority of them were found exclusively coming from the northwest direction. The majority of those in the north-northwest were located only a few degrees away from the station, whereas those in the west-northwest were located farther away.

Chapter 4

Discussion

In this chapter the possible factors for the failure of the forecasts in capturing some STT events are discussed. As shown in Section 3.4 the forecast skill deteriorates with increasing pressure levels, where below 700 hPa over half of the events were missed by the STT forecasts, albeit that for above 500 hPa was fairly accurate. The lowest level from 700 hPa to 1000 hPa roughly corresponds to the PBL and thus the failure to capture events in this region would mostly stem from the subgrid parameterization of the mixing processes in the GEM model and the ambiguities associated with it in the kinematic trajectory method (Bourqui and Trépanier 2010). The rest may be accounted for by the following potential reasonings:

1. the GEM global forecasts on which the present STT data are based may diverge significantly from the truth over 6 days due to the chaotic nature of the atmosphere,

2. the subjective determination of intrusion levels is sensitive to somewhat arbitrary parameters, and/or

3. the trajectories do not take into account the subgrid processes such as convection and turbulent mixing.

The first point stems from the nature of atmospheric dynamics and it could amplify the initial uncertainties in the model; thus it sets the theoretical limitations to the predictability of forecast models.

As for the second point, as discussed in Section 2.3 some levels of arbitrariness and subjectivity were necessarily introduced when determining the intrusion levels for each measurement profile, especially for ambiguous cases. In the process it is possible that some areas with tropospheric ozone in combination with low relative humidity were misrepresented as STT events. This however is impossible to distinguish in the absence of accompanying tracer species such as beryllium-7.

Regarding the third point, Cristofanelli et al. (2003) reported in the model intercomparison against measurement that Lagrangian trajectory method failed to capture some observed STT events likely due to its lack of convection and turbulence schemes. Gray (2003) studied the significance of such parameterized convection and turbulence mixing processes in model studies with use of a passive tracer in a mesoscale model with and without those schemes. They showed in a case study using a mature cyclone that the inclusion of such processes led to the increase of STT events by as much as 62 %, predominantly due to convective transport. Turbulent mixing, on the other hand, turned out to be an order of magnitude smaller than convective mixing. Furthermore, the convective mixing was found to be even more significant when it comes to the deep STT events, accounting for maximum of approximately 70 % of such events, by diluting the tracer concentration in vicinity of the updraft detrainment while enhancing it below the tropopause (Gray 2003). The extent of this, however, is strongly dependent on the model's convection scheme, and whether quantitatively it applies to the present study is questionable. Yet it suggests that in the worst case scenario as much as 38 % could attribute to the convection and to the lesser extent the subgrid turbulent mixing. Also, although the free troposphere is a region where turbulence is less common and only intermittently generated by the breaking of gravity waves, or the presence of convection, wind shear as well as radiation (Stohl et al. 2003), Shapiro (1980) identified that the clear air turbulence (CAT) is the primary mechanism for STE at the tropopause folds that are associated with jet stream frontal zone. Trajectories feel some of the effects of CAT through the turbulence effect on potential temperature and potential vorticity of winds across the jet. Such large scale CAT is included in our trajectory study, but the effect of CAT might be underestimated.

Also, although there is no significant bias reported for the GEM forecast model particularly associated with the region of interest, the seemingly systematic shifts towards the east as seen in Figure 3-15 may be related to the fact that Montreal is located within Saint Lawrence River valley (SLRV): A primary topography in Eastern Canada, extending from Lake Ontario to Gulf of St.Lawrence, passing Montreal and Quebec city in the southwest-northeast direction. Montreal, especially, is a region that is situated at the focus of three valleys (St. Lawrence River Valley, Lake Champlain Valley, and Ottawa River Valley), which makes the task of forecasting winds in this region particularly non-trivial owing to the complex wind channeling effect. SLRV in particular is known to cause bidirectional wind channeling in the region which strongly varies seasonally: Northeasterly and southwesterly. Carrera et al. (2009) estimated the wind climatology from 1979 to 2002 and found that during the summer (JJA) the wind in Montreal is predominantly westerly to south-westerly as shown in Figure 4-1. It is interesting to note that the petals shown in Figure 4-1 excerpted from Carrera et al. (2009) are approximately opposite to those in Figure 3-15, except for the most frequent southeast shift. This predominant westerly to southwesterly flow could have pushed, for some reasons, the clusters farther from the station by a few degrees over the trajectory calculation duration of six days. But further research is required to better understand this apparent bias.

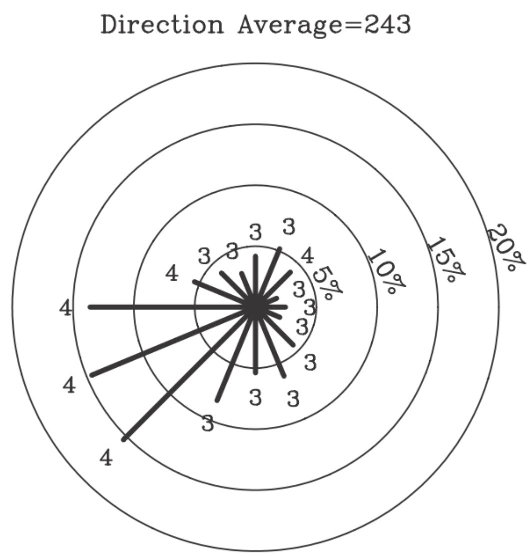

Figure 4.1: Surface wind rose diagram for Montreal for the period of 1979–2002. Excerpted from Carrera et al. (2009), their Figure 3 (c).

Chapter 5

Automation of intrusion level detection

In order to determine the bottom and top intrusion levels for any measurement profile systematically and unambiguously, as opposed to the subjective method introduced in Section 2.3, an automatic detection algorithm was developed. Such an algorithm has only been attempted, to the knowledge of the author, by Haver and Muer (1996) who, in order to identify tropopause folds, used more than 2800 observed profiles for the period of between 1969 and 1994. In their analysis they used the ozone mixing ratio relative to the climatological ozone mixing ratio as a primary criterion. In the present study, however, due to the limited number of available measurement profiles and also due to the large frequency of the observed intrusions, a climatology could not be extracted from the campaign. Also the algorithm by Haver and Muer (1996) targets only those intrusions situated around 400 hPa, thus it is not adequate for the goal of the present study of detecting STT events throughout the troposphere, including the lower troposphere. Therefore an alternative algorithm was formulated as follows:

- Bottom of the intrusions; algorithm looking upward

    1. Abrupt decrease in humidity: -$\frac{dRH}{dP} \leq$ -1 %/hPa
    and RH $\leq$ 60 % above.
    2. Abrupt increase in ozone: -$\frac{dO_3}{dP} \geq$ 0.1 ppbv/hPa

- Top of the intrusions; algorithm looking upward

    1. Abrupt increase in humidity: -$\frac{dRH}{dP} \geq$ 1 %/hPa
    and RH $\geq$ 40 % above.
    2. Abrupt decrease in ozone: -$\frac{dO_3}{dP} \leq$ -0.1 ppbv/hPa

Initially, following the subjective identification procedure, another criterion using the covariance between the relative humidity and ozone was included. Yet it was found to yield the same output without it, and was therefore excluded from the criteria. Once the levels are identified, in order to avoid successive occurrences of tops and bottoms of intrusions within short vertical distances, the levels were set so that the bottom level and the top level alternate and the intrusion is at least 50 hPa deep. In case when intrusions are found thinner than 50 hPa, the layer is disregarded. When multiple intrusions were observed in a profile, a vertical threshold distance of 50 hPa was also set between the two intrusions. If two successive intrusions are found closer together than 50 hPa, the top and the bottom of the intrusion levels for the lower and the upper intrusion layers respectively are disregarded, so that the two layers are merged into one. Note that rather large threshold values of relative humidity were used here, compared to those used by Haver and Muer (1996) of 25 %, in order to regard the region with more or less diluted stratospheric signature as a part of the intrusion layer for ambiguous cases. Those parameter values were specified carefully so that the intrusion levels found by the algorithm match those detected subjectively without significant differences.

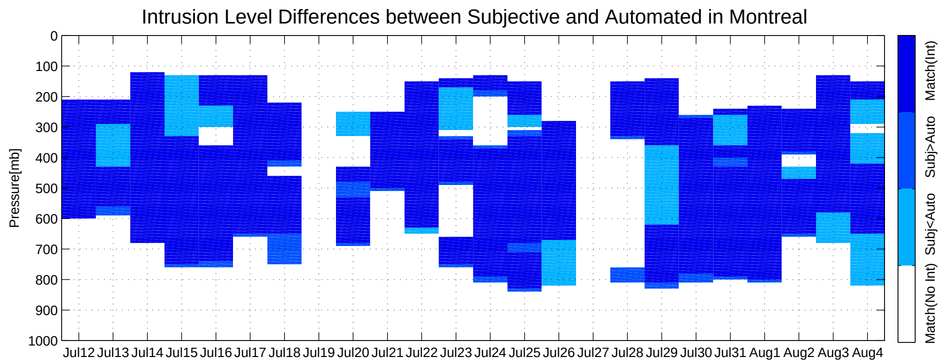

(a)

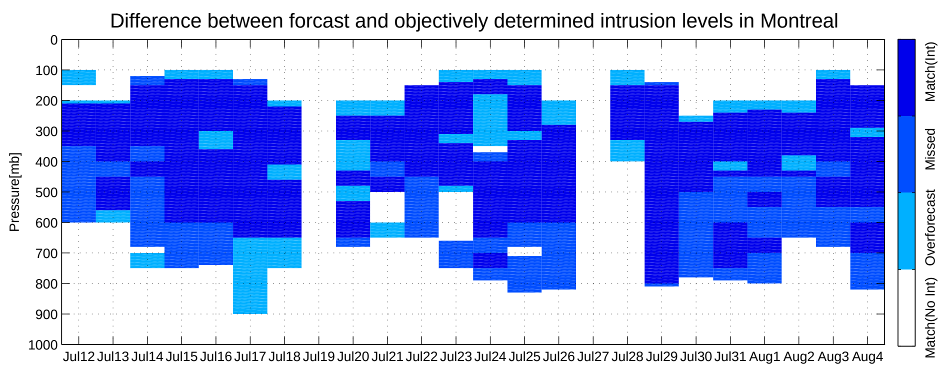

(b)

Figure 5.1: 2D histograms for each measurement day at Montreal station of (a) differences between the intrusion levels identified by the criteria described in Section 2-3 and those determined by the automated algorithm described in this section, and (b) difference between the intrusions determined by the algorithm and the STT forecast datasets. Each 10-hPa vertical bin was assigned one of the four categories as described on the side colour bar. The blank columns denote where data are missing.

Figure 5-1 (a) presents the differences between subjectively determined intrusion levels and those found by the algorithm described above. By screening it is obvious that they match fairly well, though the latter sees slightly more intrusions than the former. Quantitatively speaking, the algorithm increased the presence of intrusions by 18.1 % on average, and 18.2 % for the pressure region between 300 and 500 hPa, 9.6 % from 500 to 700 hPa, and 24.1 % from 700 to 1000 hPa. In contrast, some former intrusion layers were disregarded by the algorithm, with an overall removal of former intrusion layers being by 6.3 % on average, and for the aforementioned pressure regions 4.0 %, 5.0 %, and 25.0 %, respectively. Therefore in total more regions in the upper troposphere were taken as intrusion layers, whereas in the lower troposphere some intrusion layers were moved from one time to another.

Differences between STT forecasts and the new intrusion levels specified by the algorithm are displayed in Figure 5-1 (b). It shows that the missed layers are almost exclusively situated in the lowest part of the intrusions, as was the case for the previous detection method (Figure 3-5 (c)). The percentage of missed events found by the algorithm in comparison with the subjective intrusion detection is summarized in Table 5-1.

Pressure	$300 \leq P < 500hPa$	$500 \leq P < 700hPa$	$700 \leq P < 1000hPa$
Algorithm	15.2 %	49.1 %	77.6 %
Subjective	16.1 %	48.3 %	73.1 %

Table 5.1: The percentage of missed events found by the aforementioned algorithm relative to that of the subjective intrusion detection method during the campaign period.

Thus, the missed events decreased above 500 hPa while increased below 500 hPa only insignificantly. On the other hand, the fraction of the overforecast in contrast to those found by the subjective method is summarized in Table 5-2.

Pressure	$300 \leq P < 500hPa$	$500 \leq P < 700hPa$	$700 \leq P < 1000hPa$
Algorithm	14.1 %	6.5 %	29.9 %
Subjective	29.2 %	8.4 %	25.0 %

Table 5.2: Same as Table 5-1, but for the overforecast events.

The algorithm therefore removes some overforecast events above 700 hPa while adding some below it slightly. Hence, overall the algorithm proved to be a successful tool in automatically identifying the intrusion levels.

Chapter 6

Conclusion

In this thesis, new Lagrangian STT forecasts were closely investigated and validated against measurement profiles taken during an ozonesonde balloon campaign conducted from 12 July to 4 August 2010. The STT forecasts are calculated using a Lagrangian kinematic trajectory methodology driven by the high-resolution global forecast from the GEM model running at EC.

The balloon sonde profiles show an overall frequency of stratospheric intrusions which is much higher than expected at all three launching sites, with almost each individual profile showing the ingress of stratospheric air down to 500 hPa and about 25 to 50 % of the profiles down to 700 hPa or deeper. The same behaviour was observed in the STT forecasts, corresponding to a tenfold increase of stratospheric mass flux across 700 hPa compared to the previous study by Sprenger and Wernli (2003). As suggested by Bourqui and Trépanier (2010), who also detected a mass flux of approximately an order of magnitude larger than Sprenger and Wernli (2003), the following three factors may be responsible for this large discrepancies: (1) Misrepresentation of the STT events by Sprenger and Wernli (2003) as a result of the low spatio-temporal resolution in their model, (2) August 2006 and July/August 2010 being two anomalously active seasons, and/or (3) change in the STT annual cycle potentially related to climate change. The agreement of the present study with Bourqui and Trépanier (2010), however, most likely reduces the likelihood of (2). Another difference exists in the residence times used in each study. This mere factor, however, is unlikely to account for the observed tenfold difference, and thus further investigation is required.

Three intrusion periods, each lasting for several days, were found in both observed profiles and STT forecasts as shown in Figure 3-5, which to a rough approximation corresponds to the time-scale of baroclinic life cycle. The STT forecasts were found to agree reasonably well with the observations, albeit a tendency to underestimate STT events below 500 hPa. In addition, Figure 3-8 suggests significant dilution of stratospheric signatures with the surrounding tropospheric air during the descent into the troposphere from both specific humidity and ozone mixing ratio. Several possible factors explaining the failures of the forecasts were suggested in Chapter 4, including the divergence of GEM forecasts over 6 days, possible misinterpretation of tropospheric air as STT events, as well as the lack of the convection and turbulence parameterizations in the trajectory method. Gray (2003) found maximum of 70 % increase in deep STT events by considering deep convection, suggesting that convection could have accounted for the missed events. In spite of these limitations, the STT forecasts turn out to be reasonably accurate. The fact that essentially a half of the events were missed below 700 hPa, on the other hand, indicated that the mass flux across 700 hPa shown in Section 3.2 is underestimated by

50 %, resulting in further increase in the discrepancies compared to the past study of Sprenger and Wernli (2003). Although further research is necessary to ascertain this result, if this turns out to be general, the current view of STT events need to be revised.

Clusters in the vicinity of the Montreal station around measurement times were analysed in order to investigate the missed events. A total of 42 clusters was found in the region, a quarter of which were labelled as (ex), indicating that if they were extended for a few more days they would reach the station and thus be captured as events. Those without label (ex) and those with were separately analysed for their relative locations to the Montreal station, and it turned out that most of the clusters in the former category fell on the east side of the station, whereas the latter fell exclusively on the northwest to the west. The latter is intuitive as the predominant flow in the upper air is westerly in the region. The former, however, may be due to the fact that the Montreal station as well as the other two locations lie in the SLRV, where the complex terrain structure leads to a bidirectional wind channelling in southwesterly and northeasterly depending on the season. Carrera et al. (2009) showed that during the summer the flow is predominantly westerly to southwesterly, thus potentially explaining shift in the clusters.

Lastly, an algorithm was developed as an alternative method to the subjective determination method described in Section 2.3, in order to enable the systematic detection of stratospheric intrusion from balloon sonde profiles. The algorithm successfully detected the intrusions using relative humidity and ozone mixing ratio from measured profiles.

The STT forecasts thus validated can be used for many purposes in future studies, including the estimate of a STT global one-year climatology, to be compared with Sprenger and Wernli (2003) and Wernli and Bourqui (2002) for instance, potentially in association with climate indices such as NAO. Many climatological studies have been performed in the past for the northern hemisphere, but not for the southern hemisphere. Thus it will be interesting to see the climatology as well as the spatio-temporal variability of such events in the southern hemisphere, taking advantage of the global coverage of the dataset. Another interesting aspect would be to look at the mass flux across the 380 K isentropic surface, also available as an output of the trajectory model. The quantitative aspect along with the geographical locations of such mass flux has never been looked at on the global scale; therefore, it would not only provide a brand new climatology in that aspect but also will potentially act to bridge the two pictures of STE presented in Chapter 1, namely the small-scale-driven flux across the tropopause and the large-scale-driven driven flux across the 380 K isentrope.

Bibliography

D. J. Bamber, P. G. Healey, B. M. Jones, S. A. Penkett, A. F. Tuck, and G. Vaughan. Vertical profiles of tropospheric gases - chemical consequences of stratospheric intrusions. *Atmos. Environ.*, 18:1759–1766, 1984.

M. Beekman, G. Ancellet, S. Blonsky, D. De Muer, A. Ebel, H. Elbern, J. Hendricks, J. Kowol, C. Mancier, R. Sladkovic, H.G.J. Smit, P. Speth, T. Trickl, , and Ph. Van Haver. Regional and global tropopause fold occurrence and related ozone flux across the tropopause. *J. Atmos. Chem.*, 28:29–44, 1997.

S. Bethan, G. Vaughan, and S. J. Reid. A comparison of ozone and thermal tropopause heights and the impact of tropopause definition on quantifying the ozone content of the troposphere. *Q. J. R. Meteorol. Soc.*, 122:929–944, 1996.

M. Bithell, L. J. Gray, and B. D. Cox. A three-dimensional view of the evolution of midlatitude stratospheric intrusions. *J. Atmos. Sci.*, 56:673–688, 1999.

M. Bourqui. Stratosphere-troposphere exchange from the lagrangian perspective: A case study and method sensitivities. *Atmos. Chem. Phys.*, 6:2651–2669, 2006.

M. Bourqui and P.-Y. Trépanier. Descent of deep stratospheric intrusions during the ions august 2006 campaign. *J. Geophys. Res.*, 115, 2010. doi: 10.1029/2009JD013183.

A. W. Brewer. Evidence for a world circulation provided by the measurements of helium and water vapour distribution in the stratosphere. *Q. J. R. Meteorol. Soc.*, 75:351–363, 1949.

M. L. Carrera, J. R. Gyakum, and C. A. Lin. Observational study of wind channeling within the st. lawrence river valley. *J. Appl. Meteorol. Climatol.*, 48:2341–2361, 2009.

P. Chen. Isentropic cross-tropopause mass exchange in the extratropics. *J. Geophys. Res.*, 100:16,661–16,673, 1995.

J. Côté, S. Gravel, A. Méthot, A. Patoine, M. Roch, and A. Staniforth. The operational cmc-mrb global environmental multiscale (gem) model. part i: Design considerations and formulations. *Mon. Wea. Rev.*, 126:1373–1395, 1998a.

J. Côté, J. Desmarais, S. Gravel, A. Méthot, A. Patoine, M. Roch, and A. Staniforth. The operational cmc-mrb global environmental multiscale (gem) model. part ii: Results. *Mon. Wea. Rev.*, 126:1397–1418, 1998b.

P. Cristofanelli, P. Bonasoni, W. Collins, J. Feichter, C. Foster, P. James, A. Kentarchos, P. W. Kubik, C. Land, J. Meloen, G. J. Roelofs, P. Siegmund, M. Sprenger, C. Schnabel, A. Stohl, L. Tobler, L. Tositti, and T. Trickl. Stratosphere-to-troposphere transport: A model and method evaluation. *J. Geophys. Res.*, 108(D12):8525, 2003. doi: 10.1029/2002JD002600.

E. F. Danielsen. Stratospheric-tropospheric exchane based on radioactivity, ozone and potential vorticity. *J. Atmos. Sci.*, 25:502–518, 1968.

T. Deshler, J. L. Mercer, H. G. J. Smit, R. Stubi, G. Levrat, B. J. Johnson, S. J. Oltmans, R. Kivi, A. M. Thompson, J. Witte, J. Davies, F. J. Schmidlin, G. Brothers, and T. Sasaki. Atmospheric comparison of electrochemical cell ozonesondes from different manufacturers, and with different cathode solution strengths: The balloon experiment on standards for ozonesondes. *J. Geophys. Res.*, 113, 2008. doi: 10.1029/2007JD008975.

G. M. B. Dobson. Origin and distribution of polyatomic molecules in the atmosphere. *Proc. Roy. Soc. Lond.*, A236:187–193, 1956. doi: 10.1098/rspa.1956.0127.

A. Ebel, H.Hass, H.J.Jakobs, M.Laube, M.Memmesheimer, and A.Oberreuter. Simulation of ozone intrusion caused by a tropopause fold and cut-off low. *Atmos. Environ., Part A*, 25:2131–2144, 1991.

H. Elbern, J. Kowol, R. Sladkovic, and A. Ebel. A statistical assessment with model guided analyses. *Atmos. Environ.*, 31:3207–3226, 1997.

S. L. Gray. A case study of stratosphere to troposphere transport: The role of convective transport and the sensitivity to model resolution. *J. Geophys. Res.*, 108, 2003. doi: 10.1029/2002JD003317.

P. Van Haver and D. De Muer. Climatology of tropopause folds at midlatitudes. *Geophys. res. lett.*, 23(9):1033–1036, 1996.

J. R. Holton, P. H. Haynes, E. M. McIntyre, A. R. Douglass, R. B. Rood, and

L. Pfister. Stratosphere-troposphere exchange. *Rev. Geophys.*, 33:403–439, 1995.

B. J. Hoskins. Towards a pv-theta view of the general circulation. *Tellus, Ser. A*, 43:27–35, 1991.

B. J. Hoskins, M. E. McIntyre, and A. W. Robertson. On the use and significance of isentropic potential vorticity maps. *Q. J. R. Meteorol. Soc.*, 111: 877–946, 1985.

W. D. Komhyr. Electrochemical concentration cells for gas analysis. *Ann. Geophys.*, 25:203–210, 1969.

W. D. Komhyr, R. A. Barnes, G. B. Brothers, J. A. Lathrop, and D. P. Opperman. Electrochemical concentration cell performance evaluation during stoic. *J. Geophys. Res.*, 100:9231–9244, 1995.

J. F. Lamarque and P. G. Hess. Cross-tropopause mass exchange and potential vorticity budget in a simulated tropopause folding. *J. Atmos. Sci.*, 51:2246–2269, 1994.

J. F. Lamarque, A.O. Langford, and M.H. Proffitt. Cross-tropopause mixing of ozone through gravity wave breaking: Observation and modeling. *J. Geophys. Res.*, 101:22,969–22,976, 1996.

O. Poulida, R. R. Dickerson, and A. Heymsfield. Stratosphere-troposphere exchange in a midlatitude mesoscale convective complex: 1. observations. *J. Geophys. Res.*, 101:6823–6836, 1996.

J. D. Price and G. Vaughan. Statistical studies of cut-off-low systems. *Annales Geophysicae*, 10:96–102, 1992.

J. D. Price and G. Vaughan. The potential for stratosphere-troposphere exchange in cut-off-low systems. *Q. J. R. Meteorol. Soc.*, 119:343–365, 1993.

R. J. Reed. A study of a characteristic type of upper level frontogenesis. *J. Met.*, 12:226–237, 1955.

R. J. Reed and E. F. Danielsen. Fronts in the vicinity of the tropopause. *Archiv fur Meteorologie, Geophysik und Bioklimatologie, Ser. A*, 11:1–17, 1959.

M. A. Shapiro. Turbulent mixing within tropopause folds as a mechanism for the exchange of chemical constituents between the stratosphere and troposphere. *J. Atmos. Sci.*, 37:994–1004, 1980.

H. G. J. Smit, W. Straeter, B. J. Johnson, S. J. Oltmans, J. Davies, D. W. Tarasick, B. Hoegger, R. Stubi, F. J. Schmidlin, T. Northam, A. M. Thompson, J. C. Witte, I. Boyd, and F. Posny. Assessment of the performance of ecc-ozonesondes under quasi-flight conditions in the environmental simulation chamber: Insights from the juelich ozone sonde intercomparison experiment (josie). *J. Geophys. Res.*, 112, 2007. doi: 10.1029/2005GL024323.

M. Sprenger and H. Wernli. A northern hemispheric climatology of cross-tropopause exchange for the era-15 time period. *J. Geophys. Res.*, 108, 2003. doi: 10.1029/2002JD002,636.

M. Sprenger, M. C. Maspoli, and H. Wernli. A northern hemispheric climatology of cross-tropopause exchange for the era 15 time period (1979–1993). *J. Geophys. Res.*, 108, 2003. doi: 10.1029/2002JD002587.

A. Stohl, N. Spichtinger-Rakowskya, P. Bonasonib, H. Feldmannc, M. Memmesheimerc, H. E. Scheeld, T. Trickld, S. H*ú*benere, W. Ringerf, and M. Mandlg. The influence of stratospheric intrusions on alpine ozone concentrations. *Atmos. Environ.*, 34:1323–1354, 2000.

A. Stohl, P. Bonasoni, P. Cristofanelli, W. Collins, J. Feichter, A. Frank, C. Forster, E. Gerasopoulos, H. Gaggeler, P. James, T. Kentarchos, H. Kromp-Kolb, B. Kruger, C. Land, J. Meloen, A. Papayannis, A. Priller, P. Seibert, M. Sprenger, G. J. Roelofs, H. E. Scheel, C. Schnabel, P. Siegmund, L. Tobler, T. Trickl, H. Wernli, V. Wirth, P. Zanis, and C. Zerefos. Stratosphere-troposphere exchange: A review, and what we have learned from staccato. *J. Geophys. Res.*, 108(D12), 2003. doi: 10.1029/2002JD002490.

K. Sudo, M. Takahashi, and H. Akimoto. Future changes in stratosphere-troposphere exchange and their impacts on future tropospheric ozone simulations. *Geophys. res. lett.*, 30(24), 2003. doi: 10.1029/2003GL018526.

D. C. Thornton and N. Niazy. Sources of background current in the ecc ozonesonde: Implications for total ozone measurement. *J. Geophys. Res.*, 87:8953, 1982.

G. Vaughan. Stratosphere-troposphere exchange of ozone. In Isaksen I.S.A., editor, *Tropospheric Ozone*, pages 125–135. NATO ASI Series, Reidel, Dordrecht, 1988.

M. Y. Wei. A new formulation of the exchange of mass and trace constituents between the stratosphere and the troposphere. *J. Atmos. Sci.*, 44:3079–86, 1987.

H. Wernli and M. Bourqui. A Lagrangian "1-year climatology" of (deep) cross-tropopause exchange in the extratropical Northern Hemisphere. *J. Geophys. Res.*, 107, 2002. doi: 10.1029/2001JD000812.

H. Wernli and H. C. Davies. A lagrangian-based analysis of extratropical cyclones. part i: The method and some applicaations. *Q. J. R. Meteorol. Soc.*, 123:467–489, 1997.

V. Wirth. Thermal versus dynamical tropopause in upper troposphere balanced flow anomalies. *Q. J. R. Meteorol. Soc.*, 126:299–317, 2000.

V. Wirth and J. Egger. Diagnosing extratropical synoptic-scale stratosphere-troposphere exchange: A case study. *Q. J. R. Meteorol. Soc.*, 125:635–655, 1999.

WMO. Atmospheric ozone 1985. *WMO Global Ozone Res. and Monit. Proj. Rep. 20*, 1986.

K. Yeh, J. Côté, S. Gravel, A. Méthot, A. Patoine, M. Roch, and A. Staniforth. The cmc-mrb global environmental multiscale (gem) model. part iii: Nonhydrostatic formulation. *Mon. Wea. Rev.*, 130:339–356, 2002.